HAL open science

# The role of plasticity and hydrogen flux in the fracture of a tempered martensitic steel: A new design of mechanical test until fracture to separate the influence of mobile from deeply trapped hydrogen

D. Guedes, L. Cupertino Malheiros, A. Oudriss, S. Cohendoz, J. Bouhattate, Jordi Creus, F. Thebault, M. Piette, X. Feaugas

**To cite this version:**

D. Guedes, L. Cupertino Malheiros, A. Oudriss, S. Cohendoz, J. Bouhattate, et al.. The role of plasticity and hydrogen flux in the fracture of a tempered martensitic steel: A new design of mechanical test until fracture to separate the influence of mobile from deeply trapped hydrogen. Acta Materialia, 2020, 186, pp.133-148. 10.1016/j.actamat.2019.12.045 . hal-02505272

**HAL Id: hal-02505272**

**https://univ-rochelle.hal.science/hal-02505272**

Submitted on 21 Jul 2022

**HAL** is a multi-disciplinary open access archive for the deposit and dissemination of scientific research documents, whether they are published or not. The documents may come from teaching and research institutions in France or abroad, or from public or private research centers.

L'archive ouverte pluridisciplinaire **HAL**, est destinée au dépôt et à la diffusion de documents scientifiques de niveau recherche, publiés ou non, émanant des établissements d'enseignement et de recherche français ou étrangers, des laboratoires publics ou privés.

Distributed under a Creative Commons Attribution - NonCommercial 4.0 International License

Version of Record: https://www.sciencedirect.com/science/article/pii/S1359645419308845
Manuscript_64b94e6173cc528786880a9c025ca5b1

# The role of plasticity and hydrogen flux in the fracture of a tempered martensitic steel: a new design of mechanical test until fracture to separate the influence of mobile from deeply trapped hydrogen

D. Guedes[a,b], L. Cupertino Malheiros[a,b], A. Oudriss[a], S. Cohendoz[a], J. Bouhattate[a], J. Creus[a], F. Thébault[b], M. Piette[b], X. Feaugas[a]

[a] La Rochelle Université, Laboratoire des Sciences de l'Ingénieur pour l'Environnement, UMR CNRS 7356, Avenue Michel Crépeau, 17042 La Rochelle Cedex, France
[b] Vallourec Research Center France, 60 route de Leval, F-59620 Aulnoye-Aymeries, France

## ABSTRACT

The design of an electrochemical permeation device on a tensile machine has allowed to control the hydrogen flux and to isolate the effects of trapped and mobile hydrogen on the hydrogen embrittlement of a martensitic steel. Based on a local approach of fracture, tensile tests on several notched specimens were completed in order to investigate the impact of hydrostatic stress, equivalent plastic strain, hydrogen concentration and flux on the damage processes. Analysis of the fracture surfaces revealed that trapped hydrogen favors ductile fracture, enhancing nucleation and growth of voids by reducing the interface energy between precipitates/inclusions and matrix. Mobile hydrogen leads to quasi-cleavage along the substructure (lath and/or blocks) boundaries at mainly the {101} planes. For both mechanisms, the mutual interaction between hydrogen and dislocations (drag process increasing hydrogen diffusion and hydrogen favoring dislocations mobility) has a large contribution to the hydrogen embrittlement of the martensitic steel.

**Keywords:** hydrogen embrittlement; fracture; plasticity; martensitic steel; quasi-cleavage

© 2019 published by Elsevier. This manuscript is made available under the CC BY NC user license
https://creativecommons.org/licenses/by-nc/4.0/

**Nomenclature**

**Tests**

| | |
|---|---|
| SWH | Axisymmetric or plate specimen without hydrogen |
| PCD | Axisymmetric pre-charged and desorbed specimen |
| SUF | Plate specimen under flux |
| UFD | Plate under flux and desorbed specimen |

**Specimens**

| | |
|---|---|
| AEU | Axisymmetric U-notched specimen |
| AEV | Axisymmetric V-notched specimen |
| ATL | Axisymmetric smooth specimen |
| PNU | Plate U-notched specimen |
| PNV | Plate V-notched specimen |
| PTL | Plate smooth specimen |

**Mechanics**

| | |
|---|---|
| A | Strain sensitivity parameter |
| b | Burgers vector |
| $I_{HE}$ | Hydrogen embrittlement factor |
| Kt | Stress concentration factor |
| M | Taylor factor |
| QC | Quasi-cleavage fracture |
| V | Activation volume |
| $\varepsilon_{\phi}$ | Local plastic strain associated to the reduction of section |
| $\varepsilon_{11}$ | Engineering longitudinal strain until fracture |
| $\varepsilon_{peq}$ | Equivalent plastic strain |
| $\rho$ | Dislocations density |
| $\sigma^*$ | Relaxed stress |
| $\sigma_{eq}$ | Equivalent stress |
| $\sigma_c$ | Critical stress for fracture |
| $\sigma_f$ | Fracture stress |
| $\sigma_m$ | Hydrostatic stress |
| $\sigma_{max}$ | Maximum engineering stress |

**Hydrogen**

| | |
|---|---|
| $C_D$ | Diffusive hydrogen content |
| $C_H$ | Total hydrogen content |
| $C_{Tir}$ | Deeply trapped hydrogen content |
| $D_{app}$ | Apparent diffusion coefficient |
| J | Hydrogen flux |
| $J_0$ | Hydrogen flux at stationary state |
| $N_T$ | Number density of trapping sites |
| $N_L$ | Number density of interstitial sites |
| $\Delta E_T$ | Trapping energy |

**Others**

| | |
|---|---|
| EBSD | Electron backscatter diffraction |
| FEM | Finite element method |
| HE | Hydrogen embrittlement |
| HEDE | Hydrogen-enhanced decohesion |
| HELP | Hydrogen-enhanced localized plasticity |
| $k_B$ | Boltzmann's constant |
| SEM | Scanning electron microscope |
| TDS | Thermal desorption spectroscopy |
| TEM | Transmission electron microscope |

## 1. Introduction

Hydrogen embrittlement (HE) is a phenomenon that is increasingly mentioned during premature fracture of industrial components in service. For example, oil and gas extraction is often accompanied by the presence of hydrogen sulfide, which favors the absorption and diffusion of hydrogen into metallic alloys [1, 2]. Therefore, HE is a major concern for the development of tubular products for oil and gas production.

On a macroscopic scale, the consequences of hydrogen can be characterized by a decrease of the mechanical properties including fracture strain, fatigue life and changes of the fracture mode

[3-5]. These effects have been reported by many studies on several alloys such as nickel base alloys [6-8], stainless [9-10] and martensitic steels [11-13]. From a phenomenological point of view, without considering the case of the formation of hydrides, HE can be explained by three models. The first one is based on the assumption that hydrogen promotes plasticity, which is divided into two mechanisms: Hydrogen-Enhanced Localized Plasticity (HELP) [14] and Adsorption-Induced Dislocation Emission (AIDE) [15]. The second model is related to the reduction of cohesion energy (Hydrogen-Enhanced Decohesion, HEDE) [16]. Finally, the third model states that hydrogen promotes the formation of vacancies (Superabundant Vacancies, SAV) at high temperatures and hydrogen partial pressures [17, 18], under severe cathodic charging [19] or as a result of electrodeposition reactions [20]. The possible combination of more than one of these models has also been proposed in order to understand the HE experimental results [21].

These HE models focus on the interactions between hydrogen and metallurgical heterogeneities and are primarily the result of the decrease of defect energies due to solute segregation according to the "defactant" concept proposed by Kirchheim [22, 23]. Hydrogen seems to decrease the energies for emission and mobility of dislocations, vacancies formation and cohesion of interfaces, which may result in fracture modes with a strong contribution of plasticity and/or interfaces decohesion. It is, therefore, necessary to understand the nature of the interactions of hydrogen with structural defects. In terms of the impact of hydrogen on plasticity, the hydrogen-dislocation interactions have been the subject of numerous studies [24-31]. These works show that the elastic field at the vicinity of edge dislocations is a reversible trap for hydrogen, whereas the edge dislocation core is an irreversible trap. The trapping of hydrogen by dislocations can decrease its diffusivity, but also influence the interactions between dislocations by shielding the elastic field and promoting the emission and mobility of dislocations (HELP). According to some authors [9, 10, 32-35], these effects can lead to

plasticity localization and brittle transgranular quasi-cleavage fracture. The impact of hydrogen on the cohesion energy of interfaces can also contribute to hydrogen-assisted damage. Evidence of plasticity and decohesion mechanisms were previously observed for several metallic alloys [7, 9, 35-37].

From a metallurgical point of view, the nature, density and distribution of trap sites, such as vacancies, inclusions, precipitates and dislocations are key parameters to understand the HE [38-45]. In addition to the structure, the service mechanical request also determines the susceptibility to hydrogen-assisted cracking. Mechanical states present two components: hydrostatic and deviatoric stresses. Both affect damage and are classically formalized in terms of stress triaxiality. Notched specimens are often used to introduce variability of stress triaxiality. For instance, several authors used notched specimens to study the influence of triaxiality on nucleation and growth of the cavities in ductile fractures of steels and titanium alloys. They assume that there is a critical local stress to cavity formation, which is dependent on the hydrostatic stress and the local plastic strain [46-48].

Once hydrogen assisted-cracking happens in lath martensitic steels, intergranular and quasi-cleavage fracture surfaces are often observed [11-13, 33, 35]. The structure immediately beneath both fracture morphologies reveals an extensive plasticity with intense slip bands and disturbed lath boundaries [11]. A synergetic action of HELP and HEDE mechanisms has been proposed to explain HE in these steels [35-37]. Hydrogen associated with dislocations would promote their activity and their pile-up at the laths, blocks, packets and prior austenite grain boundaries. The hydrogen deposited by the dislocations at these interfaces (or carbides/matrix interfaces) would then lead to local decohesion.

Despite the numerous studies on HE of martensitic steels, there are still gaps in the current knowledge. The contribution of diffusive and trapped hydrogen on the damage processes is not illucidated. It is also still not clear how hydrogen promotes the quasi-cleavage fracture and the

role of plasticity in this process. The interactions between hydrogen and dislocations have not been fully understood yet. Additionally, it is still unknown if the hydrogen concentration or the flux of hydrogen impact the most the hydrogen-induced fracture. We have investigated the influence of hydrostatic stress on the hydrogen solubility, diffusivity, trapping and flux in tempered martensitic steels [49-51]. However, we have not identified the role of this hydrostatic stress component in the fracture process. Continuing these first studies, the present work aims to clarify the contributions of hydrogen flux, hydrostatic stress and plasticity to the damage mechanisms. To achieve this objective, tensile test with specimens that present several notch geometries were performed in pre-charging conditions or in an electrochemical permeation device combined with a tensile machine. Based on a local approach of fracture, the two observed damage modes (ductile and quasi-cleavage) were formalized in terms of hydrostatic stress-equivalent plastic strain ($\sigma_m$, $\varepsilon_{peq}$) maps which allowed to demonstrate at a macroscopic scale the contribution of plastic deformation to both damage processes. In order to elucidate the meaning of this contribution, we evaluated firstly the impact of plastic strain on hydrogen flux and secondly the hydrogen impact on dislocations mobility using stress relaxation tests, which provide the activation volume and barrier energy to mobile dislocations. Both analysis gave further insights about the hydrogen-dislocation interactions and their effects on the development of fracture. Based on the tests results, new considerations are raised regarding the respective contributions of trapped and diffusible hydrogen to damage.

## 2. Experimental Procedures

### *2.1 Material and Characterization*

The present work studies the Fe-0.3C-0.4Si-0.5Mn-1.0Cr-0.8Mo-0.05V-0.04Nb (weight %) martensitic steel with small amounts (less than 0.04 wt.%) of Al, S, Cu, Co and Ca. Samples of 180 x 120 x 15 mm were austenitized at 910°C for 10 min and then water quenched. Thereafter, tempering was conducted at 710°C for 30 minutes. Structural characterization was performed

using SEM coupled with EBSD and TEM following a similar methodology previously employed [40]. The steel presents a fully lath tempered martensitic structure with prior austenite grain size of 10 µm, average lath size of 0.28 µm, dislocations density of $5.2 \times 10^{14}$ $m^{-2}$ and a complex carbide precipitation state which comprises mainly η-$Fe_2C$, $Fe_3C$, $Cr_7C_3$ and $Mo_2C$ with a density of 274 $\mu m^{-3}$. Hydrogen distribution quantification was completed using electrochemical permeation (EP) test and thermal desorption spectroscopy (TDS). These procedures were described in [37, 38]. The hydrogen apparent diffusion ($D_{app}$) coefficient in the steel is $1.1 \times 10^{-10}$ $m^2/s$. Activation energies and volumetric densities of interstitial and trapping sites were obtained using the data of EP tests performed at four temperatures ranging from 283 K to 313 K. The steel contains $1.1 \times 10^{27}$ and $2.3 \times 10^{25}$ $m^{-3}$ intersticial ($N_L$) and deep trapping sites ($N_T$), respectively. The obtained activation energy for moving between adjacent interstitial sites is 0.23 eV (22.2 kJ/mol) and for moving from a deep trapping to a lattice site is 0.47 eV (45.3 kJ/mol). A detailed description of these experimental techniques has already been published in previous works [40, 41, 49-51].

*2.2. Mechanical Testing*

The local approach of fracture combines a fine analysis of mechanical state (strains and stresses numerically determined) with damage (evolution of damage and failure criteria experimentally evaluated) of highly solicited regions (Representative Elementary Volume, REV) of structures (notched specimens). In the present work, we extended this approach to the hydrogen embrittlement context with additional calculations of hydrogen distribution until fracture. Firstly, experiments on cylindrical and plate specimens (smooth or notched) are performed at several hydrogen charging conditions. Before the beginning of hydrogen charging, the specimens are mechanically polished up to SiC polishing paper grade 4000 then rinsed with ethanol and dried under a stream of dry air. The outside diameter of the cylindrical specimens (ATL, AEU, AEV) is 9 mm and the internal diameter of the notch area is 5 mm. The U-notches

(AEU specimens) have radius of 2 or 5 mm, whereas the V-notches (AEV specimens) have notch tip radius of 0.25 or 0.1 mm and angle of 60°. For the plate specimens (PTL, PNU, PNV), the overall thickness is 2.25 mm and at the notches bottom (PNU and PNV) the thickness is 1.25 mm. The U-notch (PNU specimens) has a radius of 1 mm, whereas the V-notch (PNV specimens) presents a tip radius of 0.1 mm and an angle of 60°.

Our methodology comprises four kinds of mechanical tests which allowed to separate the impact of mobile from trapped hydrogen in the plasticity and damage: (i) cylindrical or plate Specimen Without Hydrogen (SWH), (ii) cylindrical Pre-Charged and Desorbed specimen (PCD), (iii) plate Specimen Under hydrogen Flux (SUF) and (iv) Under hydrogen Flux and Desorbed plate specimen (UFD). The experimental details of the studied specimens are listed in the Table 1. For the PCD tests, cylindrical smooth (ATL), U (AEU) and V-notched (AEV) specimens were electrochemically pre-charged in molar acidic solution using a saturated sulfate reference electrode SSE ($Hg/Hg_2SO_4/K_2SO_4$) and a platinum counter electrode (Figure 1a). Constant cathodic current densities between -20 and -100 $mA/cm^2$ were applied for 24 hours in a 1 mol/L $H_2SO_4$ solution. The temperature was set at 20°C and the cell was kept under argon flux. Tensile testing was performed after a desorption step of 24 hours at the room temperature. TDS measurements were used to verify that only deeply trapped hydrogen is present after these 24 hours of desorption. Therefore, the PCD test evaluate only the impact of deeply trapped hydrogen on the mechanical properties. The concentration of deeply trapped hydrogen is measured in a reference sample charged at the same conditions and in the specimens after their fracture. The PCD results were compared to the reference specimens tested without hydrogen (SWH).

For the SUF and UFD tests, plate smooth (PTL), U (PNU) and V-notched (PNV) specimens were submitted to an EP test connected directly to the tensile machine as already described in a previous publication [49] and shown in Figure 1(b). The permeation device is composed of a

two-compartment electrolytic cell. Both compartments are equipped with saturated sulfate reference electrodes SSE ($Hg/Hg_2SO_4/K_2SO_4$) and platinum auxiliary electrodes. A floating ground Radiometer galvanostat PGP201 is used in the charging cell, whereas a Radiometer potentiostat PGP201 is employed in the detection cell. Deionized water circulated in the double jacket through a cryothermostat Lauda RK8 CS in order to maintain a constant temperature of 293 ± 0.5 K. Solutions in both cells were continuously deoxygenated by argon. At the beginning, the detection side of the specimen is potentiostatically maintained at a constant potential of −358 mV/$Hg_2SO_4/K_2SO_4$ in a 0.1 mol/L NaOH solution (pH = 12.6) for 22 h in order to stabilize the anodic current density to approximately 0.1 μA/cm$^2$. During the electrochemical permeation test, this potential allows the oxidation of the hydrogen atoms emerging from the output face, consequently the anodic current at the exit side of the specimens gives a direct measure of the hydrogen flow rate (hydrogen flux, J). During the next step, the charging side of the specimen is galvanostatically polarized at a constant cathodic current density of -20 mA/cm$^2$ or -100 mA/cm$^2$ in a 1 mol/L $H_2SO_4$ solution, which correspond to the Vomer's domain of the hydrogen evolution reaction (HER) in this solution (verified by polarization tests) [40]. Tensile tests on plate specimens (PTL, PNU, PNV) under hydrogen flux (SUF) were performed after the permeation reaches the stationary state (constant hydrogen flux) where an equilibrium is obtained between the kinetics of diffusive and trapped hydrogen. In these tests, we follow the evolution of stress and the hydrogen flux as a function of strain. On the other hand, for the under hydrogen flux and desorbed plate specimen (UFD) tests (see Table 1), the charging current density is stopped, the acid solution is released from the charging cell and the deaeration by argon is maintained. Then the desorption step is recorded. Its current density decay is sensitive to the hydrogen release and is used together with TDS measurements to determine the amounts of diffusive hydrogen $C_D$ and trapped hydrogen $C_{Tir}$ as described in our previous works [40, 52]. After the desorption step, only deeply trapped hydrogen stays in

the material. UFD tensile tests on plate specimens (PTL, PNU, PNV) were performed after the end of these desorption steps.

**Table 1:** Fracture conditions ($\sigma_{max}$, $\sigma_f$, $\varepsilon_{11}$, $\varepsilon_\phi$, $I_{HE}$, $\sigma_m$, $\varepsilon_{peq}$) and the hydrogen states ($J_0$, $C_H$, $C_D$, $C_{Tir}$) for the specimens (ATL, AEU, AEV, PTL, PNU, PNV) and tests (SWH, PCD, SUF, UFD). Hydrogen flux is given in $\mu A/cm^2$, hydrogen concentrations in wppm, strain in % and stress in MPa. $\sigma_m$ and $\varepsilon_{peq}$ are calculated at the highly solicited regions of notched and smooth specimens. For each condition, the fracture mode is specified as dimples, QC or QC with fisheyes.

| Axisymmetric Specimens | | | | | | | | | | | | | |
|---|---|---|---|---|---|---|---|---|---|---|---|---|---|
| **Sample** | **$K_t$** | **Test** | **$C_H$** | **$C_D$** | **$C_{Tir}$** | **$\sigma_{max}$** | **$\sigma_f$** | **$\varepsilon_{11}$** | **$\varepsilon_\phi$** | **$I_{HE}$** | **$\sigma_m$** | **$\varepsilon_{peq}$** | **Fracture mode** |
| **ATL** | 1 | SWH | 0 | 0 | 0 | 903 | 536 | 17 | 68 | - | 1198 | 108 | dimples |
| **ATL** | 1 | PCD | 0.3 | 0 | 0.3 | 887 | 809 | 12 | 25 | 63 | 991 | 81 | dimples |
| **AEU** | 1.3 | SWH | 0 | 0 | 0 | 1064 | 764 | 14 | 71 | - | 1278 | 82 | dimples |
| **AEU** | 1.3 | PCD | 0.7 | 0 | 0.7 | 1058 | 763 | 15 | 66 | 7 | 1238 | 75 | dimples |
| **AEU** | 1.3 | PCD | 0.8 | 0 | 0.8 | 1020 | 761 | 14 | 70 | 1 | 1268 | 80 | dimples |
| **AEU** | 1.6 | SWH | 0 | 0 | 0 | 1215 | 1030 | 7 | 43 | - | 1299 | 32 | dimples |
| **AEU** | 1.6 | PCD | 0.2 | 0 | 0 | 1206 | 1039 | 7 | 39 | 9 | 1252 | 25 | dimples |
| **AEU** | 1.6 | PCD | 0.4 | 0 | 0 | 1210 | 1036 | 7 | 35 | 19 | 1280 | 29 | dimples |
| **AEV** | 3.2 | SWH | 0 | 0 | 0 | 1576 | 1424 | 5 | 30 | - | 1416 | 9 | dimples |
| **AEV** | 3.2 | PCD | 0.2 | 0 | 0.2 | 1561 | 1415 | 5 | 32 | -7 | 1400 | 22 | dimples |
| **AEV** | 3.2 | PCD | 0.7 | 0 | 0.7 | 1564 | 1458 | 5 | 29 | 3 | 1405 | 9 | dimples |
| **AEV** | 4.6 | SWH | 0 | 0 | 0 | 1605 | 1511 | 3 | 9 | - | 1372 | 6 | dimples |
| **AEV** | 4.6 | PCD | 0.3 | 0 | 0.3 | 1588 | 1501 | 2 | 8 | 11 | 1371 | 6.5 | dimples |

| Plate Specimens | | | | | | | | | | | | | | |
|---|---|---|---|---|---|---|---|---|---|---|---|---|---|---|
| **Sample** | **$K_t$** | **Test** | **$J_0$** | **$C_H$** | **$C_D$** | **$C_{Tir}$** | **$\sigma_{max}$** | **$\sigma_f$** | **$\varepsilon_{11}$** | **$\varepsilon_\phi$** | **$I_{HE}$** | **$\sigma_m$** | **$\varepsilon_{peq}$** | **Fracture mode** |
| **PTL** | 1 | SWH | - | 0 | 0 | 0 | 884 | 798 | 19 | 76 | - | 1141 | 79 | dimples |
| **PTL** | 1 | UFD | - | 0.6 | 0 | 0.6 | 885 | 853 | 9 | 15 | 80 | 955 | 63 | dimples |
| **PTL** | 1 | UFD | - | 1.5 | 0 | 1.5 | 884 | 825 | 11 | 9 | 88 | 1010 | 71 | dimples |
| **PTL** | 1 | SUF | 2.0 | 0.8 | 0.2 | 0.6 | 891 | 883 | 9 | 61 | 20 | 1096 | 78 | QC fisheyes / dimples |
| **PTL** | 1 | SUF | 5.5 | 2.0 | 0.5 | 1.5 | 886 | 877 | 6 | 50 | 34 | 751 | 47 | QC fisheyes / dimples |
| **PNU** | 1.3 | SWH | - | 0 | 0 | 0 | 1428 | 1352 | 0.6 | 23 | - | 1309 | 30 | dimples |
| **PNU** | 1.3 | UFD | - | 0.3 | 0 | 0.3 | 1414 | 1383 | 0.6 | 19 | 17 | 1298 | 29 | dimples |
| **PNU** | 1.3 | UFD | - | 2.0 | 0 | 2.0 | 1399 | 1373 | 0.5 | 13 | 43 | 1157 | 13 | dimples |
| **PNU** | 1.3 | SUF | 3.0 | 0.5 | 0.2 | 0.3 | - | - | - | 15 | 35 | 1230 | 21 | QC fisheyes |
| **PNU** | 1.3 | SUF | 6.7 | 2.4 | 0.4 | 2.0 | 1402 | 1380 | 0.5 | 9 | 61 | 1131 | 11 | QC fisheyes |
| **PNV** | 3.2 | SWH | - | 0 | 0 | 0 | 1575 | 1382 | 0.7 | 34 | - | 1540 | 31 | dimples |
| **PNV** | 3.2 | UFD | - | 0.4 | 0 | 0.4 | 1571 | 1515 | 0.6 | 29 | 15 | 1450 | 22 | dimples |
| **PNV** | 3.2 | UFD | - | 2.0 | 0 | 2.0 | 1569 | 1496 | 0.6 | 25 | 27 | 1420 | 20 | dimples |
| **PNV** | 3.2 | SUF | 2.1 | 0.7 | 0.3 | 0.4 | 1524 | 1414 | 0.6 | 17 | 50 | 1421 | 26 | QC |
| **PNV** | 3.2 | SUF | 8.1 | 2.2 | 0.2 | 2.0 | 1361 | 1359 | 0.3 | 12 | 65 | 1377 | 2.5 | QC |

To summarize, cylindrical PCD (ATL, AEU, AEV) and plate UFD (PTL, PNU, PNV) tests allow to evaluate the impact of deeply trapped hydrogen on damage processes. The comparison of these tests with the ones conducted at the stationary state of the permeation test (SUF) enable to separate the contributions of the mobile from the trapped hydrogen to the HE of the martensitic steel. As a reference, for all the specimens design, tensile tests in air without hydrogen pre-charging (SWH) were also performed.

All the tensile tests were conducted at a strain rate of $10^{-5}$ $s^{-1}$ in an INSTRON 100 kN machine. An extensometer was fixed onto the samples to measure the longitudinal strain ($\varepsilon_{11}$) on a gauge length of 10mm.

A summary of our experimental procedure is shown in Figure 1 and Table 1. We have reported for all the specimens (cylindrical and plate with and without notches): the stress concentration factor (Kt), the test conditions (SWH, PCD, UFD, SUF), the ultimate tensile strength ($\sigma_{max}$), the fracture stress ($\sigma_f$), the strain until fracture ($\varepsilon_{11}$), the local plastic strain until fracture ($\varepsilon_\phi$ in Equation 1), the hydrogen embrittlement index ( $I_{HE}$ in Equation 2), the hydrostatic stress ($\sigma_m$) and the equivalent plastic strain until fracture ($\varepsilon_{peq}$). $Section_f$ and $section_0$ refer to the final and initial areas of the specimens' sections, whereas $\varepsilon_\emptyset^H$ is the localized deformation for the specimens tested with hydrogen.

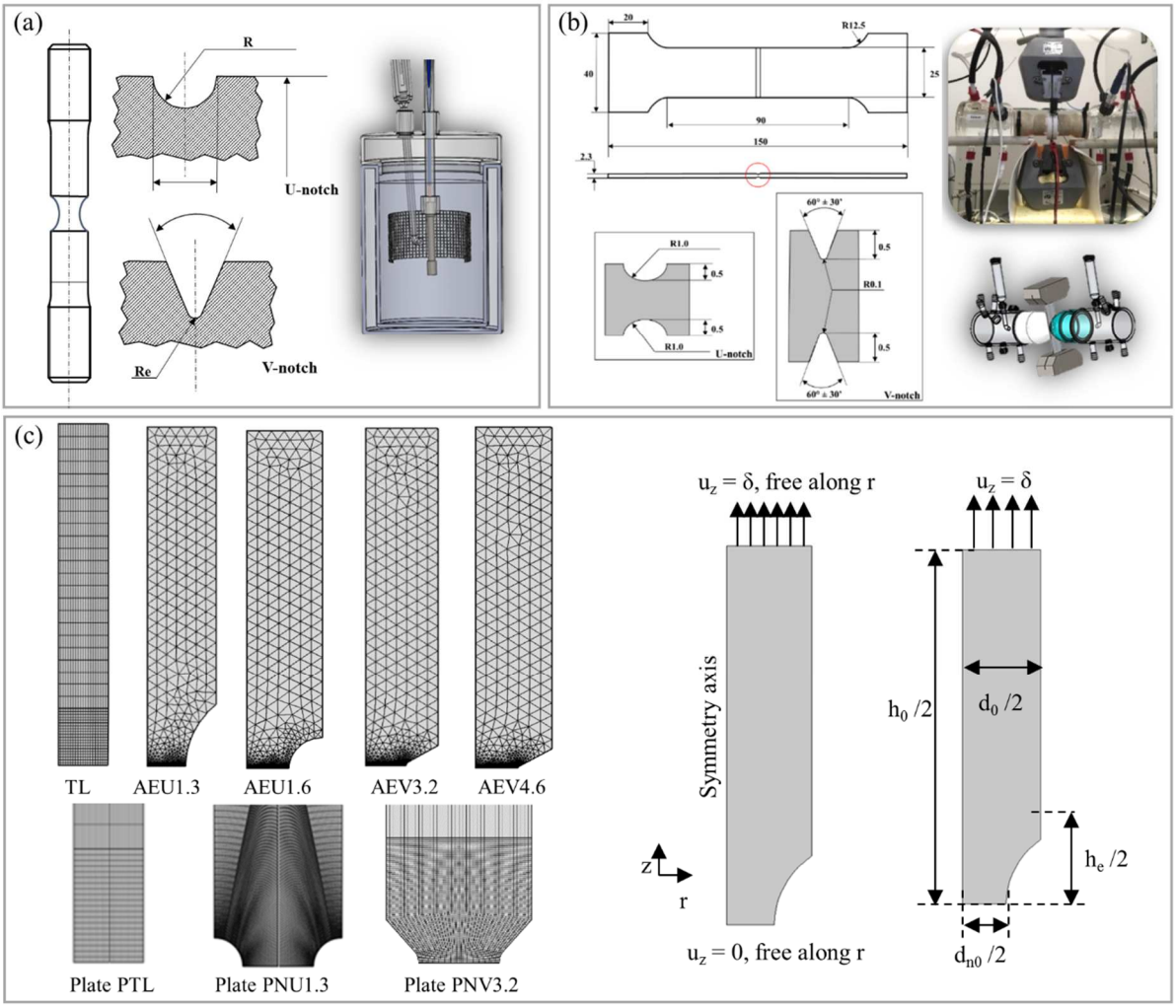


**Figure 1:** Representation of the specimens' design, charging conditions and tests with (a) pre-charged cylindrical and (b) under hydrogen flux prismatic specimens. (c) Geometries, meshes and boundary conditions of FEM calculations.

$$(\varepsilon_{\emptyset} = -\ln\left(\frac{section_f}{section_0}\right) * 100) \tag{1}$$

$$I_{HE} = 1 - \left(\frac{\varepsilon_{\emptyset}^{H}}{\varepsilon_{\emptyset}}\right) * 100 \tag{2}$$

A hydrogen analyzer Jobin Yvon Horiba EMGA-621W was used to measure the hydrogen concentration by TDS. These measurements, performed in all the studied conditions, allowed to evaluate the hydrogen content in terms of total hydrogen concentration ($C_H$), diffusive hydrogen concentration ($C_D$) and deeply trapped hydrogen content ($C_{Tir}$) as seen in Table 1.

In addition to the tensile tests previously described, relaxation tests were performed at different strain levels for specimens without hydrogen and under hydrogen flux in order to obtain the

activation volume and viscous stress (relaxed stress), which characterize the thermally activated mechanisms of plastic deformation [53, 54]. The results of these relaxations enabled us to question the impact of hydrogen on the dislocation mechanisms.

*2.3 Fracture Observations*

Transverse and longitudinal views of the fracture surfaces were observed using the SEM Philips FEI: Quanta 200FEG/ESEM, 20kV. Thereafter, a nickel layer was electrodeposited in order to protect the fracture surface during the following mechanical polishing (up to 0.02 µm colloidal silica suspension). EBSD orientation maps of the cross section of a quasi-cleavage fracture surface were performed similar to the procedure conducted by Shibata *et al*. [55]. TSL OIM software was used for the EBSD data collection and posterior analysis.

*2.4 - Numerical model - Plasticity, Diffusion and Trapping Equations*

Finite element calculations (FEM) were performed for each specimen design to provide mechanical and hydrogen distribution within the bulk up to fracture, assuming $J_2$ flow theory with isotropic and kinematic hardening [56] and diffusion-trapping model [57]. Numerical calculations are computed with the finite element software Comsol Multiphysics. During loading, the mesh is reorganized to take into account the displacement. An elastoplastic law is identified from the plastic behavior of the alloy before necking in the framework of the classical elastoplastic theory [56, 58, 59]. The validity of the FEM calculations was checked by comparing the calculated variations of engineering stress vs average longitudinal engineering strain and specimens' radius vs displacement until fracture with the experimental values. While the ductility (total elongation) is affected by the hydrogen content and mobility, the hardening law of the material is not modified through the different tests since all the curves are superimposed until necking (Figure 2). Consequently, our approach do not consider any modification of the elasto-plastic law by hydrogen.

The effect of hydrostatic stress ($\sigma_m$) on the diffusion equation is a well-known process [28, 29, 50, 57, 60, 61], which is included in our calculation to evaluate the impact of the mechanical state in the hydrogen distribution for all the tested conditions. The set of employed equations is briefly described below.

*Plasticity equations* - The elastoplastic law was identified within the framework of the classical elastoplastic theory, based on the thermodynamics of irreversible processes with internal variables [56, 59]. The stress was computed from the total strain $\bar{\bar{\varepsilon}}$ and the plastic strain $\bar{\bar{\varepsilon}}_p$ through the Hooke's law: $\bar{\bar{\sigma}} = \bar{\bar{\bar{\bar{c}}}}(\bar{\bar{\varepsilon}} - \bar{\bar{\varepsilon}}_p)$ where $\bar{\bar{\bar{\bar{c}}}}$ is the isotropic tensor of elastic moduli. The plastic potential is written as a yield function $f = J_2(\bar{\bar{\sigma}} - \bar{\bar{X}}) - \sigma_{eff} = 0$ with $J_2(\bar{\bar{\sigma}} - \bar{\bar{X}}) = \sqrt{\frac{3}{2}(\bar{\bar{S}} - \bar{\bar{X}}):(\bar{\bar{S}} - \bar{\bar{X}})}$, $\bar{\bar{S}}$ is the deviatoric part of the stress tensor $\bar{\bar{\sigma}}$ and $\sigma_{eff} = R + k$. The plastic strain is deduced from the normality rule and the definition of equivalent plastic strain rate $\dot{p}$: $\dot{\bar{\bar{\varepsilon}}}_p = \dot{p}\frac{\partial f}{\partial \bar{\bar{\sigma}}}$ and $\dot{p} = \sqrt{\frac{2}{3}\dot{\bar{\bar{\varepsilon}}}_p:\dot{\bar{\bar{\varepsilon}}}_p}$. In these equations, k is the yield stress, $R = Q(1 - \exp(-bp))$ is the isotropic hardening and $\bar{\bar{X}} = \bar{\bar{X}}_1 + \bar{\bar{X}}_2$ where $\dot{\bar{\bar{X}}}_i = \frac{2}{3}C_i\dot{\bar{\bar{\varepsilon}}}_p - \gamma_i\bar{\bar{X}}_i\dot{p}$ with $i \in \{1,2\}$ represents the kinematic hardening. The mechanical behavior is defined using nine variables E, ν, k, Q, b, $C_1$, $C_2$, $\gamma_1$, $\gamma_2$ with values are equal to 210 GPa, 0.3, 770 MPa, 2.2 GPa, 27,0.9 GPa, 0.82 GPa, 8, 7, respectively.

*Diffusion and Trapping equations* - In the present work, we consider the contributions of deeply trapped hydrogen ($C_{Tir}$) and mobile hydrogen ($C_L$) to the diffusion. The employed equations are simplifications of diffusion and trapping models described in previous works [38, 57]:

$$J = -Dapp\left(\nabla C_D - \frac{V_H}{RT}C_L\nabla\sigma_m\right) \; where \; D_{app} = D_L/\left(1 + \frac{\partial C_{Tirr}}{\partial C_L}\right)) \quad (3)$$

And

$$C_{Tir} = N_T/1 + \frac{N_L}{K_T C_L} \; with \; K_T = \exp\left[\frac{-\Delta E_T}{k_B T}\right] \quad (4)$$

$D_L$ is the interstitial diffusion coefficient, $D_{app}$ is the apparent diffusion coefficient, $\Delta E_T$ is the trapping energy, $K_T$ is a constant related to the trapping energy, $k_B$ is the Boltzmann constant, T is the temperature, $N_T$ and $N_L$ are the number of trapping and interstitial sites. We do not distinguish reversibly trapped and interstitial hydrogen. The mobile hydrogen $C_L \approx C_D$ comprises both of them, which is a limitation of our analysis. The diffusion/trapping behavior is defined using five variables $D_L$, $N_L$, $N_T$, $\Delta E_T$, T with values are equal to $1.3\times10^{-9}$ $m^2/s$, 847176 $mol/m^3$, 38.2 $mol/m^3$, - 0.26 eV, 300 K, respectively.

## 3. Results

### *3.1 Mechanical behavior*

The mechanical tests provide information on the impact of hydrogen content ($C_H$) and stress concentration (Kt) on the damage processes. We investigated the effect of notch geometry and hydrogen state (mobile or trapped) on the mechanical behavior of cylindrical in Figure 2(a) and plate specimens in Figures 2(b, c). The experimental details of the testing are listed in Table 1. As can be seen in the tensile curves of unnotched axisymmetric and plate specimens (SWH), the steel has a yield strength of approximately 820MPa, ultimate tensile strength of 900MPa and strain until fracture around 18%. For the notched specimens, the higher the $K_t$, the higher the strength ($\sigma_{max}$ and $\sigma_f$) and the smaller the strain until fracture (Figure 2, Table 1). This classical effect highlight the impact of the hydrostatic stress on damage.

In all the tests, the embrittlement effect of hydrogen was observed with the decrease of the strains ($\varepsilon_{11}$, $\varepsilon_\phi$) more than the stress values ($\sigma_{max}$, $\sigma_f$). No clear impact on the stress-strain curves was observed which suggest that, at a macroscopic scale, hydrogen does not affect the hardening behavior (Figure 2). The influence of trapped hydrogen was investigated on axisymmetric (PCD red curves in Figure 2a) and plate (UFD red curves in Figures 2b and c) desorbed specimens. For both, axisymmetric and plate specimens, the trapped hydrogen impact

is more evident for the unnotched specimens with a considerable reduction of strain until fracture ($\varepsilon_{11}$). On the other hand, mobile hydrogen effect was investigated on the SUF tests of plate specimens as shown in the blue curves of Figures 2(b) and (c). A higher embrittlement effect compared to deeply trapped hydrogen (pre-charged specimens - PCD and UFD - in Table 1 and Figure 2) was observed for all the stress concentration factors.

The local strain associated with the reduction of the section ($\varepsilon_{\phi}$) is a measure of the steel ductility chosen to calculate the hydrogen embrittlement factor, $I_{HE}$ (Equations 1 and 2). The values listed in Table 1 indicate that the $I_{HE}$ increases with the hydrogen concentration $C_H$. Additionally, deeply trapped hydrogen ($C_{Tir}$) seems to have a greater embrittlement effect promoting fracture (larger values of $I_{HE}$) mainly for low Kt values, where the plasticity is greater (see PCD and UFD tests in Table 1). On the other hand, diffusive hydrogen $C_D$ (see SUF tests in Table 1) is related to higher $I_{HE}$ when the stress concentration factors (Kt) are large, which suggest that hydrostatic stress ($\sigma_m$) promotes the damage. In order to explain these opposite results between the impacts of mobile and deeply trapped hydrogen, we have characterized the fracture surface using SEM (Figures 3 to 5).

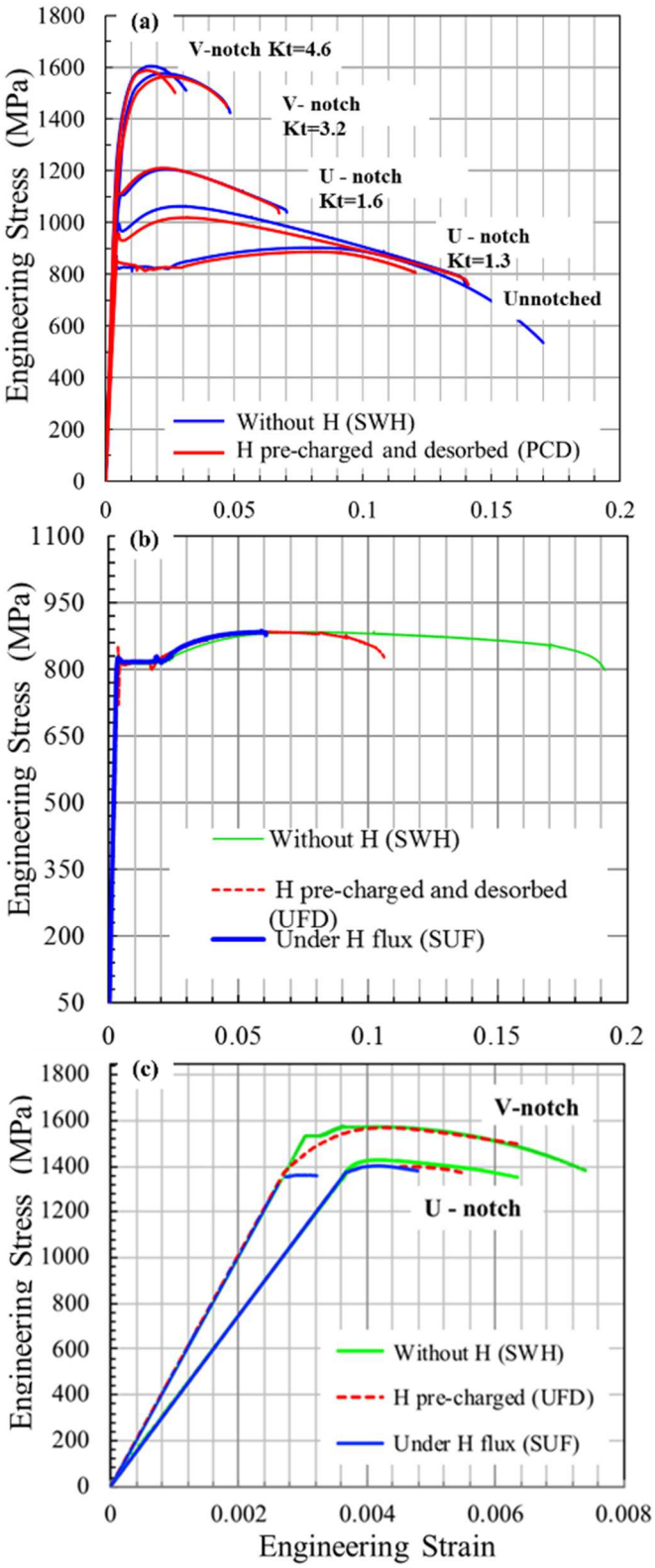


**Figure 2**: Stress-strain curves of (a) cylindrical SWH and PCD specimens, plate (b) unnotched and (c) notched SWH, UFD and SUF specimens. For all the curves, the applied cathodic current was 100mA/cm$^2$.

According to the local approach of fracture, for any damage mode, two physical parameters are key to the embrittlement process: the hydrostatic stress and the equivalent plastic strain. For

each case, the most critical locations (with the highest values of hydrostatic stress and equivalent plastic strain) inside the specimens are selected from the numerical results. For smooth and U specimens, the center of the fracture surfaces is observed, since the maximum of hydrostatic stress and equivalent plastic strain are found in the core of the specimen. Concerning the V specimens, the observation of the fracture surface is performed close to the crack tip, where the hydrostatic stress is maximum.

Deeply trapped hydrogen in PCD or UFD specimens does not change the fracture mode. The fracture surfaces of the specimens tested with (PCD and UFD) and without hydrogen pre-charging (SWH) were entirely ductile with the presence of dimples (Figure 3, Table 1). They present bimodal distributions of dimples (larger ones varying from 10 to 20 µm and smaller ones from 0.6 to 1.4 µm). These values suggest that the larger and smaller dimples are associated with inclusions (Figures 3a, b, c and d) and with precipitates (Figures 3e, f), respectively. It is possible to see inclusions in the center of large dimples highlighted with a red circle in Figure 3(d) and a small carbide in the center of a small dimple also highlighted with a red circle in Figure 3(f).

A statistical analysis of the dimple sizes enabled to demonstrate that the size of the two populations increases with Kt and with hydrogen concentration (Figure 4). The main impact of hydrogen was observed for the low Kt values and seems to be negligible at the highest Kt values. These results suggest that trapped hydrogen seems to favor the nucleation and growth of cavities around inclusions and precipitates when a large plasticity occurs.

For the specimens tested under hydrogen flux (PTL-SUF, PNU-SUF, and PNV-SUF), quasi-cleavage fracture morphology is observed where the hydrostatic stress and plastic strain are maximum in the samples. Figure 5 illustrates these observations. For smooth plate (PTL-SUF) and U- notched specimens (PNU-SUF), quasi-cleavage was observed as fish-eyes in opposite to V-notched samples (PNV-SUF) for which the mechanical parameters are maximum close to

the notch tips and we observed continuous quasi cleavage zones. Close to the edges (outside the dashed lines in Figure 5c) there are quasi-cleavage regions, whereas inside the dashed lines the fracture surface remains ductile. For each case, a higher magnification micrograph of the quasi-cleavage (Figure 5) reveals features at the scale of martensitic blocks and laths, which indicates that this type of fracture may be associated to their boundaries as suggested in previous works [35, 55].

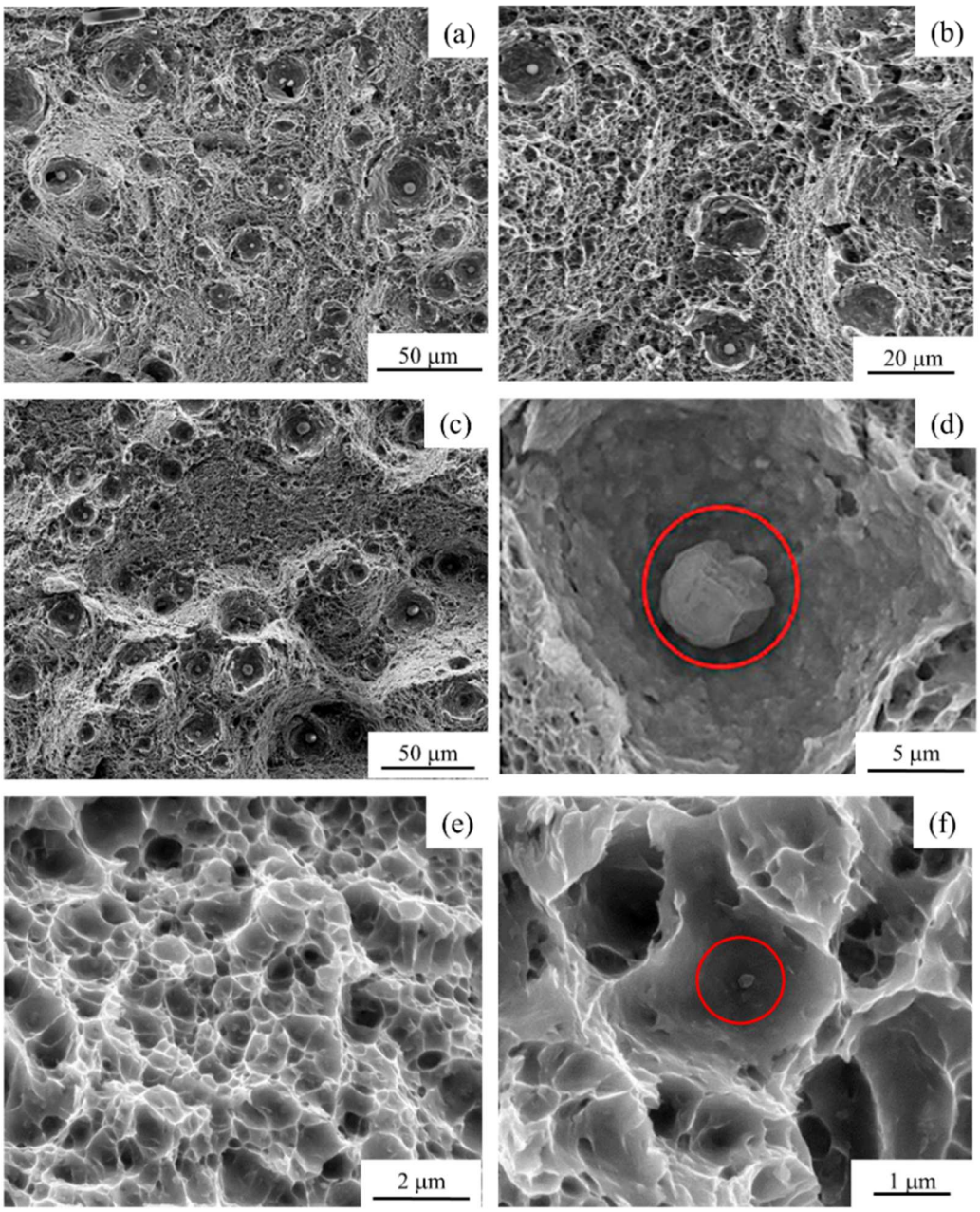


**Figure 3:** Fracture surfaces of cylindrical specimens: (a) un-charged smooth (ATL-SWH), (b) un-charged U-notched Kt=1.6 (AEU-SWH), (c) charged U-notched Kt=1.6 and $C_H$=0.4 wppm (AEU-PCD), (d) $Al_2O_3(CaO)_x$ inclusion associated with a large dimple of a smooth specimen, (e) smaller dimples and (f) carbide associated with a small dimple of charged U-notched specimen (Kt=1.6 and $C_H$=0.4 wppm).

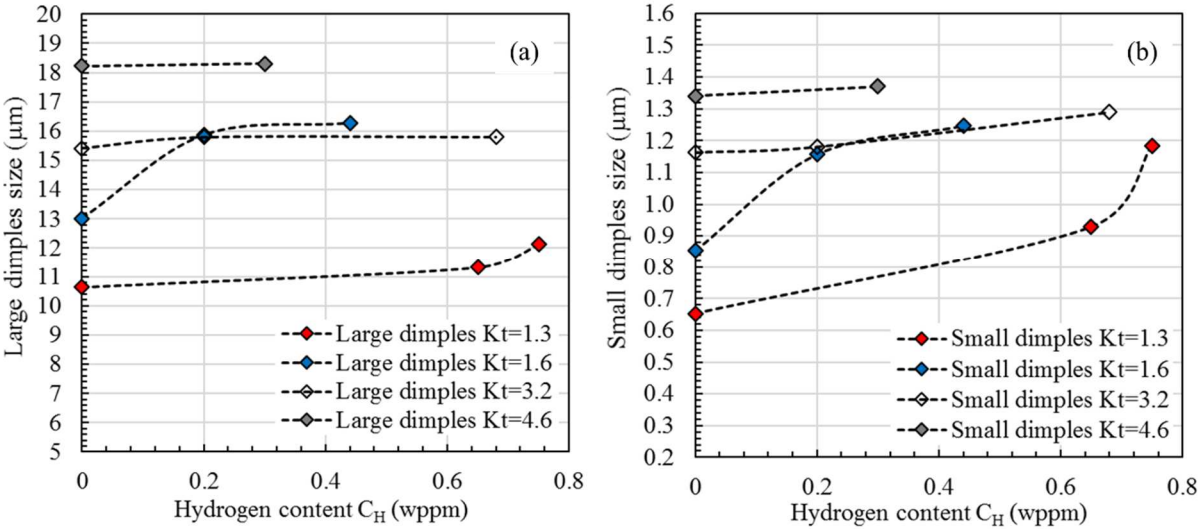


**Figure 4:** Evolution of (a) large and (b) small dimple sizes as a function of hydrogen content for several Kt.

Figure 6(a) shows a cross section of the fracture surface of a V-notched under flux specimen covered with Ni plating. The EBSD IPF map of the area inside the dashed black rectangle of the image 6(a) is displayed in Figure 6(b). In the several analyzed scans, 21 out of 34 blocks present planes of the {101} family parallel to the fracture surface. The second most presented plane family is the {100} with 10 blocks. These planes are slip and cleavage planes of the martensitic crystallographic structure, respectively. The {101} planes can be also interfaces between laths and blocks. The graphs of Figure 6(c) and 6(d) show the interface lengths and the angles between the plane normal and the tensile axis. More than 80% of the lengths are smaller than 1.2 µm with predominance of lengths between 0.3 and 0.6 µm. These values are similar to typical laths, sub-blocks and blocks sizes. The angles are more dispersed, but the majority are inferior to 30° with a peak below 10°, which cannot be considered as favorable orientation for slip activity. Therefore, both graphs suggest that the quasi-cleavage happens with the decohesion of substructure interfaces with a predominant effect of the normal stress to the fracture plane.

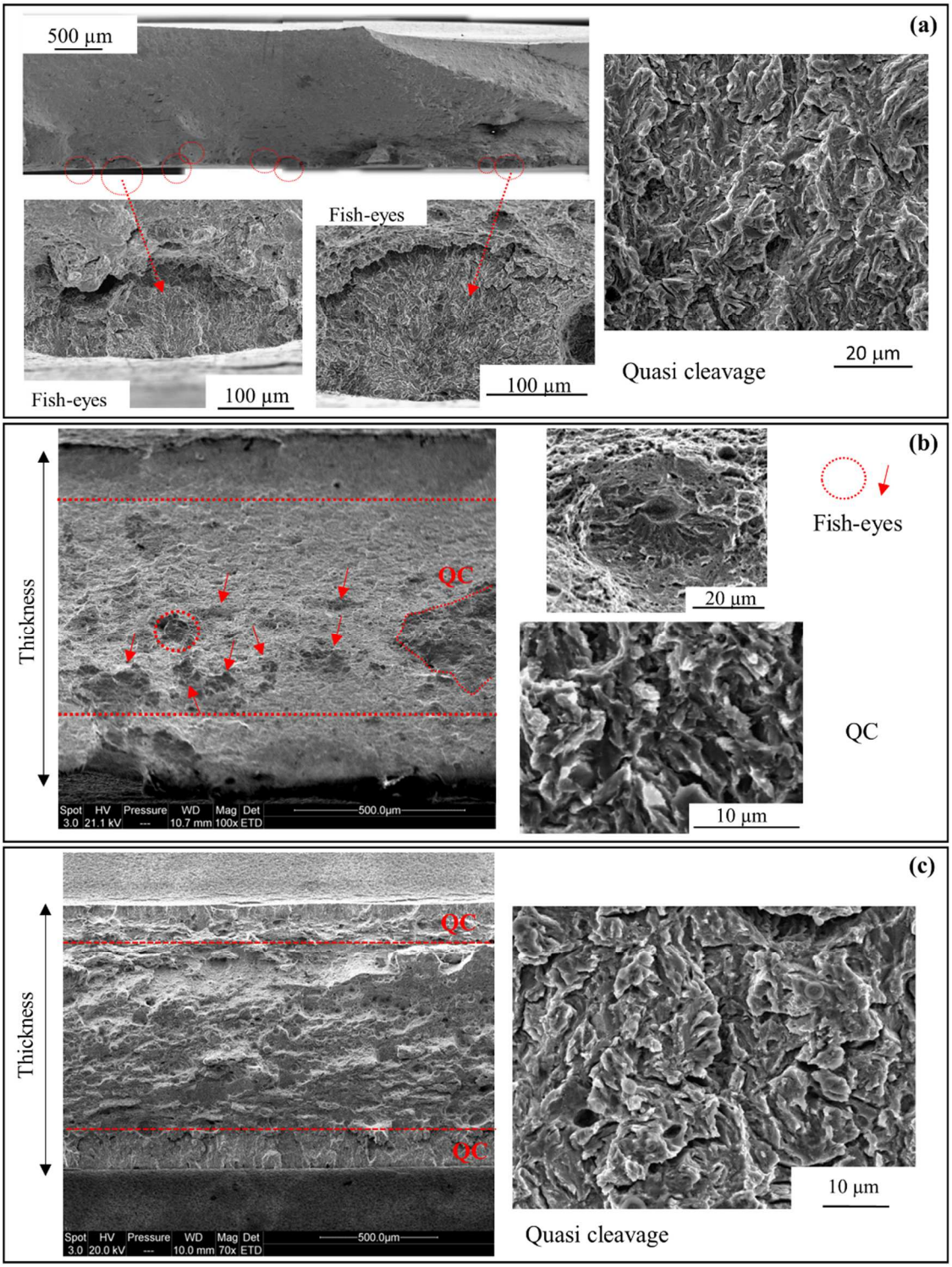


**Figure 5:** Fracture surfaces of specimens tensile tested under hydrogen flux until fracture (100 mA/cm$^2$) : (a) QC and fisheyes near the surface of smooth specimen (PTL-SUF), (b) QC and fisheyes in the bulk of U-notched specimen (PNU-SUF), (c) QC near the surface of V-notched specimen (PNV-SUF).

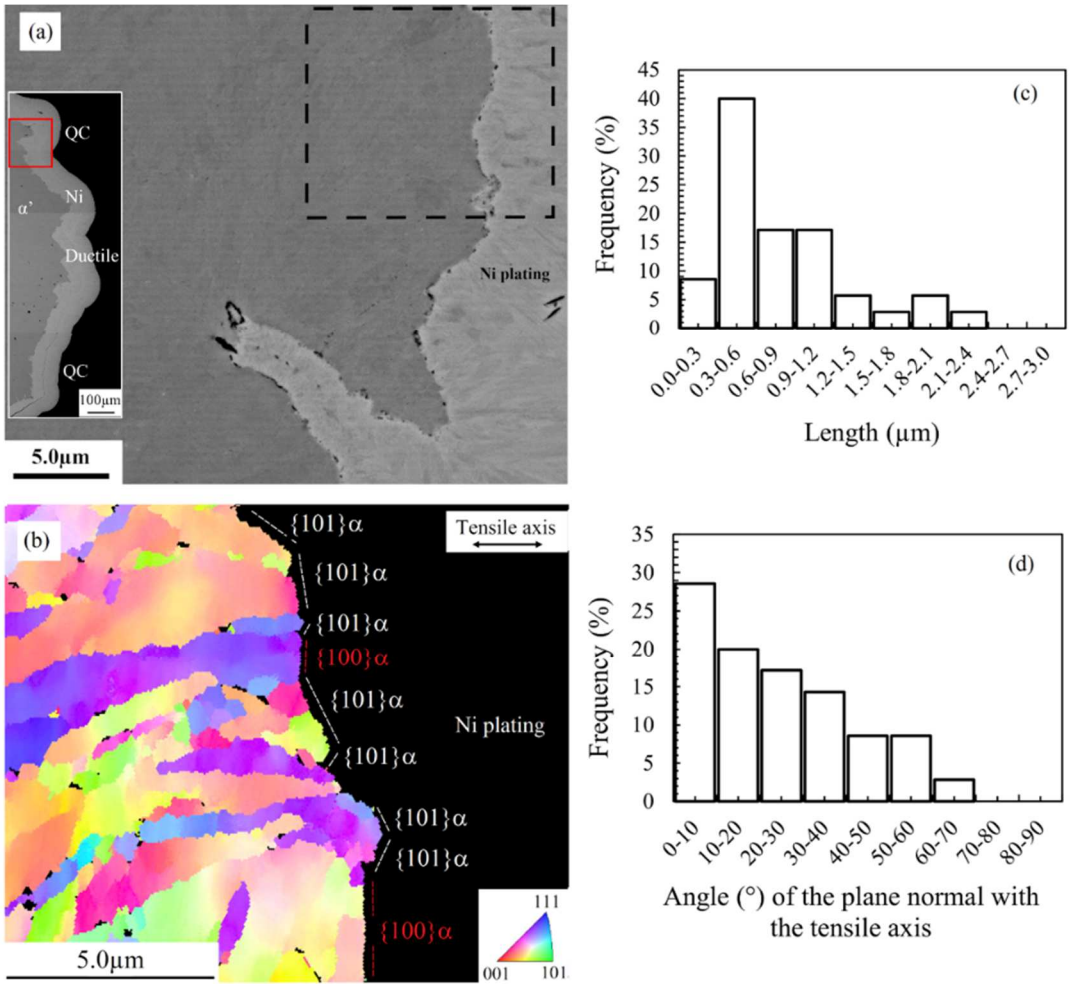


**Figure 6:** (a) SEM image and (b) corresponding EBSD IPF map of the vicinity of a fracture surface of a V-notch under hydrogen flux specimen (100 mA/cm$^2$ and $C_H = 2$ wppm). Frequencies of (c) length and (d) angle between plane normal and tensile axis.

### *3.2 Local Approach of Fracture*

Local approach of fracture refers to methodologies used to characterize the macroscopic fracture behavior in terms of hydrostatic stress ($\sigma_m$) and von Mises equivalent plastic strain ($\varepsilon_{peq}$) reached at the highly solicited regions of notched samples. They have been largely described to steels and titanium alloys for a wide range of loading conditions and crack geometries [47, 58, 62, 63, 64]. In this work, an elasto-plastic model with one isotropic and two kinematic hardening coefficients was identified independently on the hydrogen content (as described in the section 2.4) and implemented into a finite-element code. Further information is available in Reference [63]. Finite element calculations were performed for each specimen design to provide the distribution of mechanical parameters ($\sigma_m$, $\varepsilon_{peq}$) in the bulk of the

specimens during loading. Figure 7 illustrates these calculations for an ATL (a to c) and PNU (d to f) specimens. These first calculations do not include a component of hydrogen diffusion. They are based on the experimental observation that hydrogen reduces the fracture strains of the stress-strain curves. It is considered that this effect of hydrogen can be reproduced by calculating the local $\sigma_m$ and $\varepsilon_{peq}$ for the corresponding experimental maximum (fracture) strain.

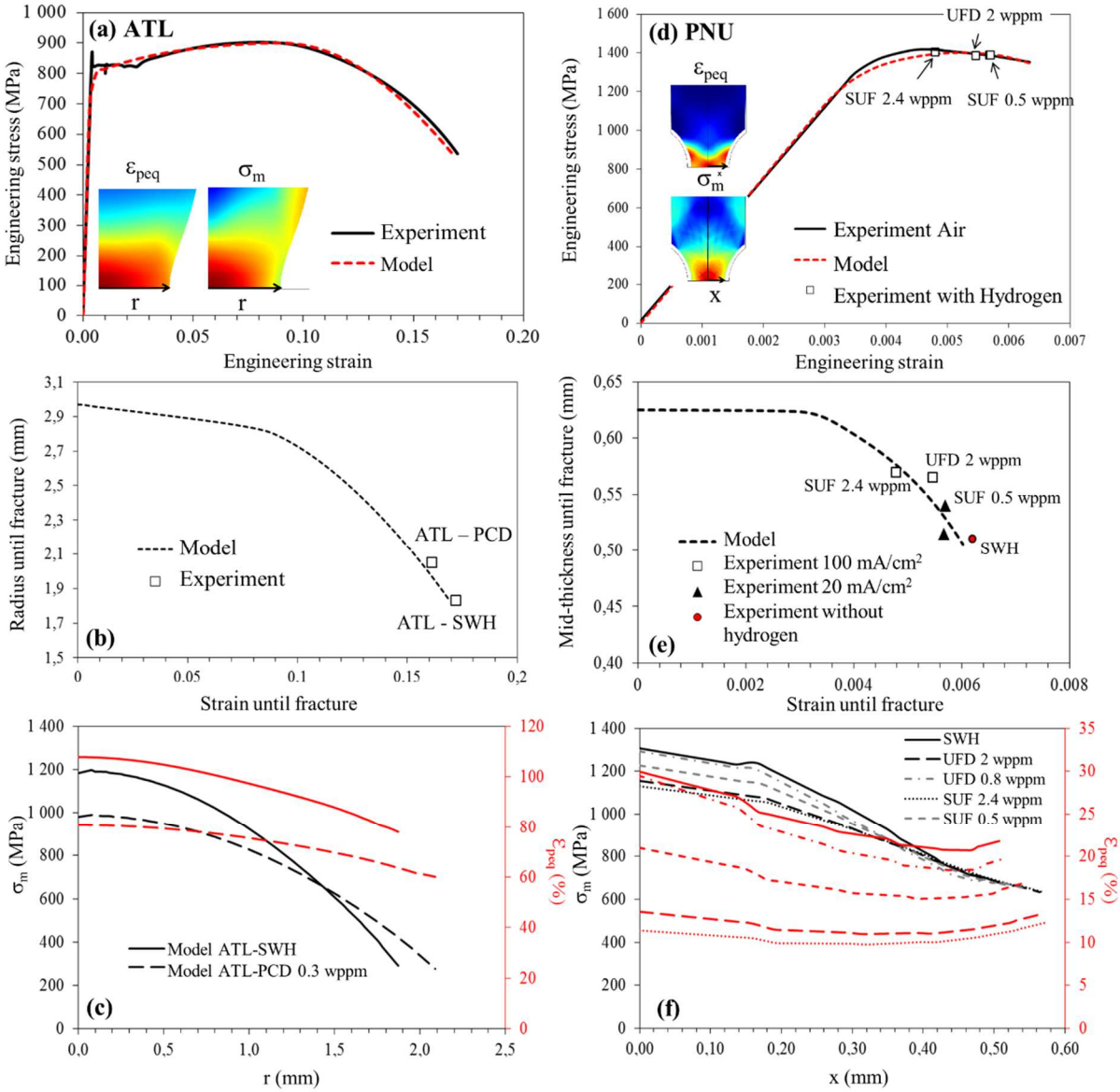


**Figure 7:** Two examples of our calculations: (a,b,c) tensile loading of ATL-SWH and ATL-PCD (0.3 wppm) and (d,e,f) PNU (Kt = 1.3) SWH, SUF and UFD. (a,d) Experimental and model engineering stress-strain curves, (b,e) predictions of the reduction of section until fracture, (c, d) $\sigma_m$ and $\varepsilon_{peq}$ along a cross-section.

Figure 8 shows the evolution of the local maximum calculated values of $\sigma_m$ and $\varepsilon_{peq}$ required for fracture at the highly solicited regions of notched samples for the three tests conditions (air (SWH), pre-charged (PCD, UFD) and under hydrogen flux (SUF)). For all the conditions, $\sigma_m$

decreases with $\varepsilon_{peq}$. A linear relationship is proposed to evaluate the dependence between these values as described by Equation 5. In this equation, A is the strain sensitivity parameter and B is a constant that represents the stress necessary for fracture in the absence of plastic deformation.

$$\sigma_m = B + A\varepsilon_{peq} \tag{5}$$

From the linear regression equations of Figure 8, it is possible to see that B slightly decreases with hydrogen (around 2% and 5% for the pre-charged and under flux conditions, respectively), whereas the absolute value of A increases considerably with hydrogen (approximately 67% and 442% for the pre-charged and under flux conditions, respectively). This indicates that mobile hydrogen increases the contribution of plasticity to the fracture process more significantly than the deeply trapped one.

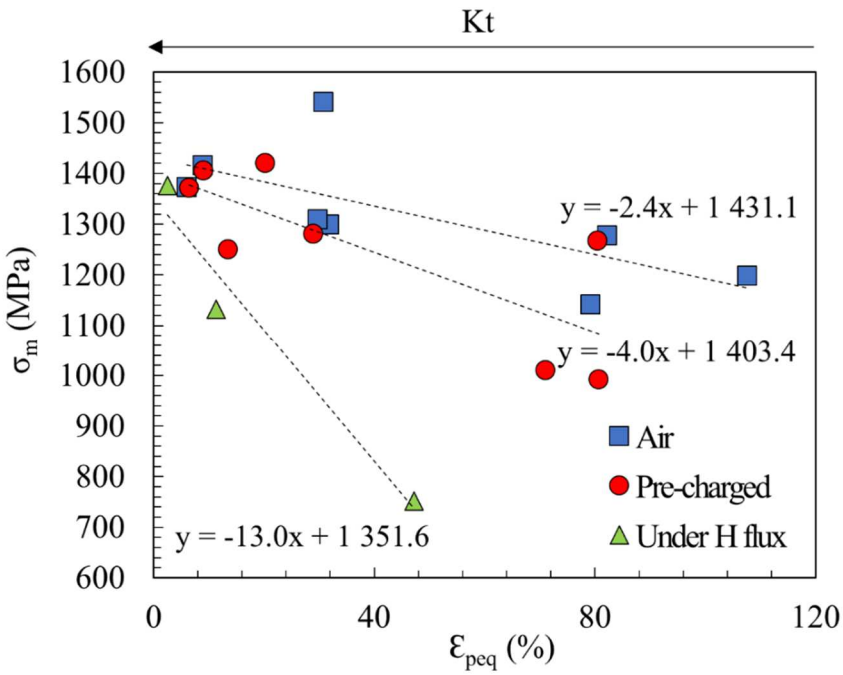


**Figure 8:** Evolution of $\sigma_m$ with $\varepsilon_{peq}$ for the highly solicited regions of the specimens at the fracture for the three tests conditions: in air (SWH), pre-charged (UFD, PCD) and under hydrogen flux (SUF) with the applied cathodic current of 100 mA/cm$^2$ and $C_H$ around 2±0.5 wppm.

In the case of quasi-cleavage fracture promoted by mobile hydrogen (SUF tests), the Equation 3 represents a macroscopic criterion of "quasi-brittle" fracture where B is the critical stress for fracture ($\sigma_c$). A decrease of this value means that the interfacial energy of the laths (or another martensitic boundary, e.g., blocks and packets) are affected by hydrogen.

For ductile fracture, the crack initiation needs to be characterized in order to evaluate the impact of hydrogen on the B parameter. SEM images of the cross sections of the ductile fracture surfaces were used to study crack initiation in the specimens without hydrogen (SWH) and pre-charged (PCD, UFD). For instance, Figure 9(a) shows the cross section of a plate V-notched specimen with voids originated around inclusions (Figure 9(b)). These voids appear to define the border between the damaged and non-damaged regions. Thus, in Figure 9(a), red lozenges locate the voids found further from the fracture and a red dashed line limits the border formed by them. The local calculated $\sigma_m$ and $\varepsilon_{peq}$ at this border is then used to plot the graph of Figure 9(c) for the damage initiation similarly to the graph of Figure 8 for the fracture. In the same way as in Equation (5), a linear relationship can be used to describe the experimental data. Again, hydrogen decreases the decohesion stress $\sigma_c$ (stress for $\varepsilon_{peq}$=0) and increases the strain sensitivity parameter (increase of the slop of $\sigma_m$ vs $\varepsilon_{peq}$). This result combined with the observations of Figure 4 suggests that the increase of plasticity contribution to the fracture process due to trapped hydrogen (pre-charging) is accomplished by favoring the crack initiation around inclusions.

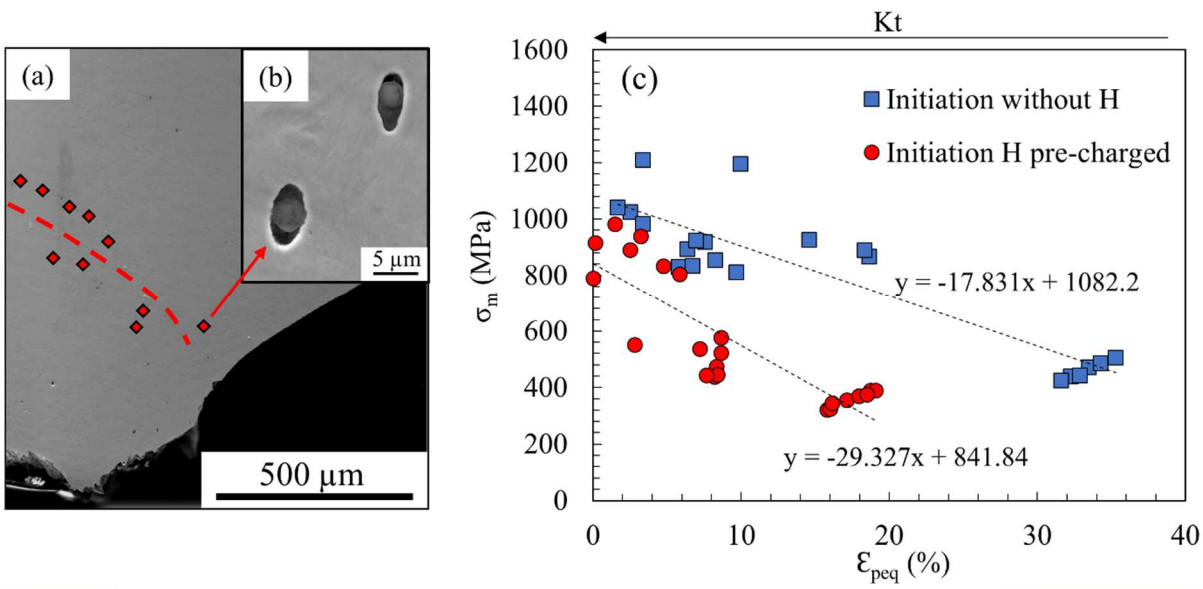


**Figure 9:** (a) Longitudinal section of a plate V-notched specimen without hydrogen showing the position of the voids found further from the fracture (red lozenges) which define the border between damaged and non-damaged regions (red dashed line), (b) magnified view of the same section showing voids around inclusions and (c) evolution of $\sigma_m$ with $\varepsilon_{peq}$ (model evaluation) at the damaged/non-damaged borders for specimens with (UFD) and without hydrogen pre-charging (SWH).

In order to demonstrate the impact of hydrogen flux on the quasi-cleavage process, we used FEM calculations to determine the hydrogen flux, i.e., J(x) profile along the cross-section of plate specimens until fracture. The elastoplastic model was then combined with hydrogen diffusion and trapping equations described in the Section 2.4, enabling to relate the hydrostatic stress ($\sigma_m$) with hydrogen flux (J) and diffusive hydrogen concentration ($C_D$). Figure 10 shows the distributions of ($\sigma_m$, $\varepsilon_{peq}$) and hydrogen concentration ($C_D$) and flux (J) for the case of V-notch specimens with the notch at (i) the hydrogen entry side, (ii) both entry and exit sides and (iii) the exit side of the permeation test, e.g., entry is the charging cell side and exit is the detection cell side.

For the case (i), the maximum values of $\sigma_m$, $\varepsilon_{peq}$, $C_D$ and J correspond to the location where the quasi-cleavage fracture was observed, i.e. near the entry surface.

For the case of the double-notched specimen (ii), the quasi-cleavage is observed in the entry and exist sides. In this case, $\sigma_m$, $\varepsilon_{peq}$, $C_D$ and J are maximum near the entry side, whereas near the exit side only $\sigma_m$, $\varepsilon_{peq}$ and J are maximum and $C_D$ is low.

Finally, in the case (iii), there is an extremely high hydrogen concentration $C_D$ and low hydrogen flux J at the entry side without notch and the quasi-cleavage is not observed next to this surface. In opposite, the notched exit side presents a zone with quasi-cleavage, where there is a high level of hydrogen flux (J) and low hydrogen concentration ($C_D$). These results, especially the cases (ii) and (iii), suggest that hydrogen flux more than hydrogen concentration promotes the brittle quasi-cleavage fracture morphology.

To sum up, our results show that deeply trapped hydrogen favor the nucleation and growth of voids favoring ductile damage conducting to fracture surfaces with dimples similar to the ones observed in the absence of hydrogen. On the other hand, diffusible hydrogen favor the quasi-cleavage process at packets, blocks or laths interfaces depending on the stress concentration

and the hydrogen flux. In both cases, the fracture criterion ($\sigma_m$ versus $\varepsilon_{peq}$) are affected by hydrogen.

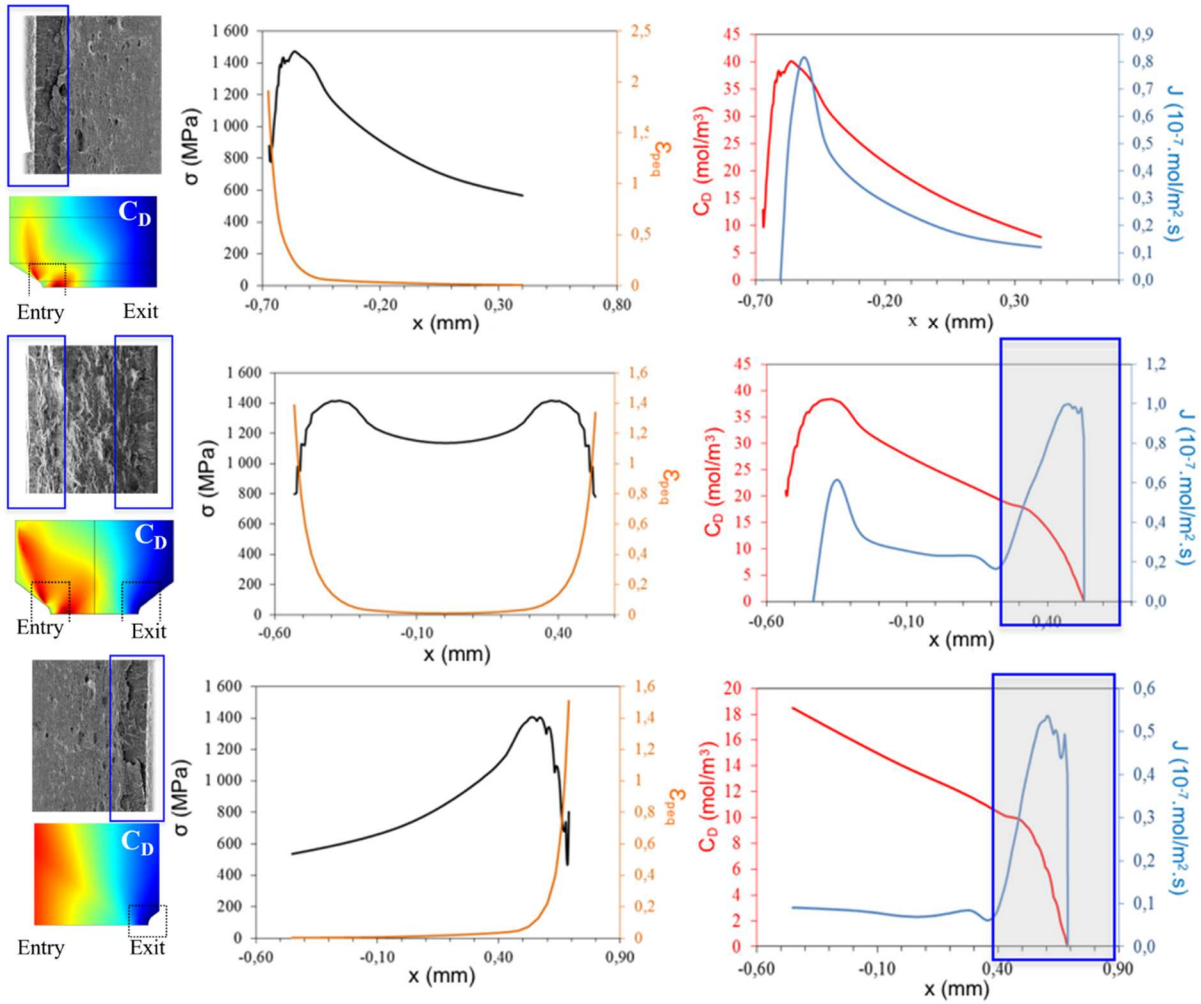


**Figure 10:** Fracture surfaces, σm, εpeq, $C_D$ and J distributions of the specimens (SUF test) with (i) a V-notch on the hydrogen entry side, (ii) V-notches on the entry and exit sides and (iii) a V-notch on the hydrogen exit side of the permeation test. On the $C_D$ maps, red corresponds to the highest values and blue to the smallest ones. The specimens were charged using cathodic current of 100mA/cm$^2$.

## 4. Discussion

In this work, mechanical testing with unnotched and notched specimens at three different conditions (without hydrogen (SWH), pre-charged (PCD, UFD) and under flux (SUF)) were performed for plate and cylindrical design of specimens. These experiments aimed to investigate the hydrogen impact in the damage process for a quenched and tempered martensitic steel. Ductile and quasi-cleavage fractures are analyzed in terms of the contributions of hydrostatic stress and plasticity. The mechanical tests performed under flux or in pre-charging

conditions allowed to separate the contributions of deeply trapped hydrogen from the diffusible hydrogen.

*4.1 Ductile Fracture*

We observed a ductile fracture morphology (dimples) for the studied steel in a large hydrostatic stress range ($\sigma_m$<1600 MPa). The nucleation of damage occurs at the interfaces of inclusions and precipitates for all the mechanical conditions ($\sigma_m$, $\varepsilon_{peq}$), resulting in a bimodal distribution of dimples. The incorporation of deeply trapped hydrogen content (in a range of up to 2 wppm) does not modify the fracture mode but impacts the voids nucleation and growth processes. The stress at the interface of a non-deformable inclusion ($\sigma_i$) can be expressed by Equation 6 [47, 58]. In this equation, $\lambda$ is a constant that depends on the inclusion shape and orientation.

$$\sigma_i = \sigma_m + \lambda E_p \varepsilon_{peq}, where\ E_p = \frac{d\sigma_{eq}}{d\varepsilon_{eq}} \quad (6)$$

The damage initiation criterion observed in Figure 9 indicates that the critical stress for interface decohesion is reduced by the presence of hydrogen ($\sigma_i$ is equal to 1082 and 841 MPa without and with deeply trapped hydrogen (2 wppm), respectively). The value of $\sigma_i$ is in agreement with the literature data related by François *et al.* [64]. The decrease of $\sigma_i$ with hydrogen suggests that hydrogen segregate to inclusions-matrix and precipitates-matrix interfaces and reduces the interface energy. Recent works have investigated the hydrogen segregation at the interface of these defects [43, 65]. As high-energy interfaces present dislocations and vacancies that allow the misfit accommodation, it is not surprising that they are able to trap hydrogen. The graph of Figure 9 also demonstrates that $E_P$ (Equation 4) increases with trapped hydrogen (considering $\lambda$ constant), facilitating the damage initiation ($\lambda E_P$ is equal to 18 and 29 MPa without and with hydrogen, respectively). The increase of $E_P$ may be related to the strain-hardening of the martensitic matrix. The presence of hydrogen segregated near or in the core of the dislocations could produce a local hardening that is not perceptible at a macroscopic scale.

Concerning cavity growth process, we did not characterize the evolution of the average cavity size but only measured the sizes of the dimples after the fracture of the specimens. These sizes seem to be higher with the addition of deeply trapped hydrogen especially for high plastic strain and low triaxiality (low stress concentration values), which supports the idea that the observed differences are a consequence of the hydrogen impact on the elementary plasticity processes.

*4.2 Quasi-cleavage Fracture*

Quasi-cleavage zones appeared in the studied steel when hydrogen flux was applied and at the locations with higher hydrostatic stress and plastic strain. Deeply trapped hydrogen was not able to promote this type of fracture. Therefore, quasi-cleavage fracture is only associated with mobile hydrogen. Oudriss *et al*. have already correlated the quasi-cleavage morphology with hydrogen mobility [66]. By studying a martensitic steel submitted to different baking times, they observed a relationship between quasi-cleavage fracture and high rates of hydrogen desorption for smooth specimens.

The EBSD analysis of the present study showed that most of the blocks at the quasi-cleavage have their planes (crystallographic family {101}) almost parallel to the fracture surface. A similar observation was previously reported by Shibata *et al*. [55]. They explained that the {101} planes correspond to boundaries between adjacent blocks and laths. Therefore, hydrogen-assisted fracture initiate and propagate along these boundaries as a cleavage. Additionally, by performing TEM immediately beneath the fracture surface, Nagao *et al*. observed that most of the quasi-cleavage fracture path seems to follow lath boundaries [33, 35]. Consequently, they also suggested that the quasi-cleavage fracture occur along blocks and/or laths boundaries. Geng *et al*. found similar results using first-principle calculations, which indicates that hydrogen can lead to decohesion between {101} planes of martensite [67]. The mechanisms of plasticity in lath martensite in the absence of hydrogen have been further studied and some authors observed sliding of substructure boundaries easily orientated for shear stress

(near 45° to the stress axis) by performing *in-situ* micro-tensile tests. They suggest that besides the crystallographic slip, plasticity at the substructure boundaries are also responsible for the overall plastic deformation [68]. In the present work, the size and the orientation (near 90° to the stress axis) of the structural features along the crack path support the idea that the fracture happened by lath and/or blocks boundaries decohesion. As the orientation is nearly perpendicular to the stress axis, it is unlikely that the interface sliding contributes to the fracture. The role of hydrogen in the quasi-cleavage fracture development is not clear since the macroscopic fracture criterion depends on the hydrostatic stress and on the equivalent plastic strain. It could be either by facilitating the decohesion of substructure boundaries (HEDE) or promoting dislocation slip and pile up (HELP) against these boundaries or even a combination of both (HEDE coupled with the HELP mechanism). The $\sigma_m$ *versus* $\varepsilon_{peq}$ graph of Figure 8 demonstrates that $\sigma_c$ is slightly lower with mobile hydrogen ($\sigma_c$ is equal to 1431MPa and 1351 MPa for without and with mobile hydrogen respectively), which support the idea that in the absence of plastic deformation a part of mobile hydrogen contributes to reduce the interface energy of blocks/laths boundaries (HEDE). In addition to this effect, mobile hydrogen enhances the contribution of plasticity to the fracture process significantly (the slope of $\sigma_m$ *versus* $\varepsilon_{peq}$ increased, A of Eq. 5 is equal to 2.4 and 13 for without and with mobile hydrogen respectively). This result confirms the hypothesis that hydrogen/plasticity interactions can contribute to the development of quasi-cleavage fracture, agreeing with the HELP mechanism. Previous observations of intense dislocation activity using TEM beneath hydrogen-induced quasi-cleavage fracture corroborate the idea that plasticity can promote the development of this fracture mode [33, 35, 36].

FEM calculations predicts a correspondence between quasi-cleavage zones and maximum hydrostatic stress, plastic strain and hydrogen flux (Figure 10). Consequently, the hydrogen flux more than hydrogen concentration is associated with the quasi-cleavage of the studied steel.

This explain why quasi-cleavage does not develop in hydrogen pre-charged specimens at the conditions explored in the present work, confirming that only mobile hydrogen contributes to the appearance of this fracture morphology. The importance of plasticity and hydrogen flux to the quasi-cleavage fracture suggests that the interactions between dislocation and mobile hydrogen are related to this fracture morphology. Dislocations are known to have a dual effect on hydrogen. Mobile dislocations can transport hydrogen facilitating their diffusion (dragging as solute atmospheres by edge dislocations) and increase the hydrogen flux [69, 70], whereas storage dislocations (dislocations tangles, walls, cells) are hydrogen trap sites reducing the hydrogen apparent diffusion coefficient [28, 29]. This dual effect was observed experimentally in this work and was correlated to plastic strain levels (Figure 11). The Figure 11(a) presents an example of the evolution of the hydrogen flux in plastic regime during a strengthening of plate smooth sample. The drag effect (hydrogen Cottrell atmospheres transport by edge dislocations) is dominant at lower levels of plastic strain where mobile dislocations multiplication occurs more significantly. The increase of hydrogen flux in this domain is an evidence of hydrogen transport by mobile dislocations. With the development of plastic deformation, there is a decrease of mobile dislocation density and an increase of storage dislocations [71], which can explain the dominance of trap phenomena at dislocations tangles and the decrease of the hydrogen flux. It was also observed that hydrogen flux is smaller for pre-strained specimens (Figure 11b). As the pre-straining reduces the density of mobile dislocations and increases the storage dislocations, this result supports the idea that mobile dislocations drag hydrogen significantly, accelerating its diffusion. As illustrated by Figure 11b, the drag process is reduced when we increase the strain rate (the increase of the flux is lower for a strain rate equal to $10^{-3}$ $s^{-1}$ than $10^{-5}$ $s^{-1}$) which suggest that the impact on damage is lower. To conclude, hydrogen transport by edge dislocations may increase the hydrogen concentration at the blocks/laths boundaries reducing their interface energy (Figure 13).

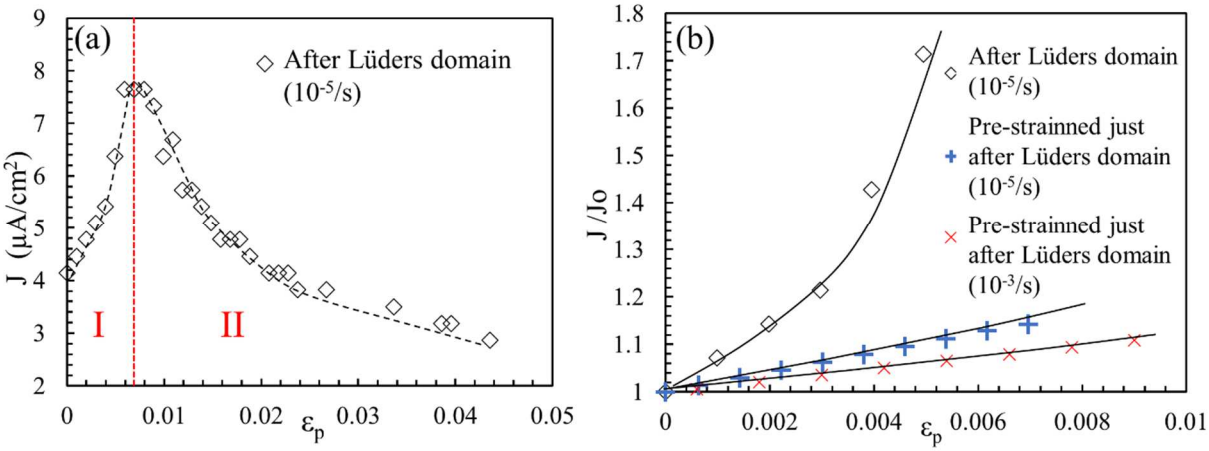


**Figure 11**: (a) Hydrogen flux evolution with plastic deformation from the end of the Lüders band and (b) normalized hydrogen flux evolution at small levels of plastic deformation highlighting the effects of pre-straining and strain rate. Tests were performed with applied cathodic current density of 100 mA/cm$^2$.

The second contribution of the hydrogen-plasticity interaction to the quasi-cleavage can be directly associated to the shielding process and consequently to the HELP model. The relaxation tests performed under hydrogen flux in the plastic regime were used to access the impact of hydrogen on thermodynamic conditions favoring the movement of dislocations. As previously described for engineering elastic regime of uncharged martensitic steel [49], we performed relaxation tests for different plastic strains and determined the activation volume (Equation 7) and relaxation stresses σ* (Figure 12).

$$V = Mk_BT\left[\frac{\partial \ln(\dot{\varepsilon}_p}{\partial \sigma}\right] \tag{7}$$

M is the Taylor factor equal to 2.5, $k_B$ is the Boltzmann's constant $1.38.10^{-23}$ J.K$^{-1}$ and T = 300K. The relaxation tests were used to identify the dislocations mechanisms with and without hydrogen flux. Two domains are observed on the curves $\dot{\varepsilon}_p$ *versus* stress (Figure 12a) in a direct relationship with the slip activity of edge and screw dislocations. The slopes are used to measure the activation volumes $V_1$ and $V_2$ for the relaxation experiments with and without hydrogen flux. Figure 12(b) shows the evolution of the normalized activation volumes $V_1/b^3$ and $V_2/b^3$ as a function of the maximal stress for both domains and both conditions. In the presence of hydrogen flux, the activation volumes decrease as previously observed for iron [30]. Figures 12(c) and 12(d) relate the evolution of the normalized activation volumes $V_1/b^3$ and $V_2/b^3$ as a

function of $1/{\sigma_1}^{*2}$ and $1/{\sigma_2}^{*1/2}$ respectively for domains I and II. In domain I, the linear relationship (Figure 12c) suggests a forest-hardening process in accordance with a pinning model of edge dislocations (Equation 8) [72, 73]:

$$\frac{V}{b^3} = \left(\frac{\pi}{8}\right)[M\alpha\mu k]^2(\sigma^*)^{-2} \tag{8}$$

where α is the elastic interaction coefficient, μ the shear modulus and k a constant relative to the pinning distance, expressed as $k/\sqrt{\rho}$ in the specific case of a forest dislocation distribution (ρ is the dislocation density). The small difference observed between both conditions (with and without flux) suggest a minor impact of mobile hydrogen on the area swept by a dislocation in the specific case of a forest edge dislocation distribution. In the domain II, the linear relationship (Figure 12d) is consistent with a kink-pair mechanism associated with the mobility of screw dislocations (Equation 9), where h is a jump distance between two equilibrium states [49, 72-74].

$$V/b^3 = [M\mu h^3/(8\pi b^3)]^{1/2} \times (\sigma^*)^{-1/2} \tag{9}$$

The decrease of the slope observed under hydrogen flux indicates a direct impact of mobile hydrogen on the jump distance h of screw dislocations which is reduced from 0.8 nm to 0.6 nm for without and with hydrogen flux, respectively. The main result is that for a same viscous stress (σ*) the activation volumes are lowered under hydrogen flux for both domains. This softening effect is confirmed by the evaluation of the activation enthalpy at the early stage of plasticity. In the domain *I,* this energy $\Delta H^* = \sigma^* V$ is equal to 0.06 eV and 0.04 eV for without hydrogen and under flux conditions (edge dislocation mobility). In the domain II, the enthalpy energy is equal to 0.28 eV and 0.15 eV for without hydrogen and under flux conditions (screw dislocation mobility). Therefore, we can conclude that mobile hydrogen reduces the dislocation jump distance of screw dislocations significantly and the activation enthalpies for both edge and screw dislocations movement.

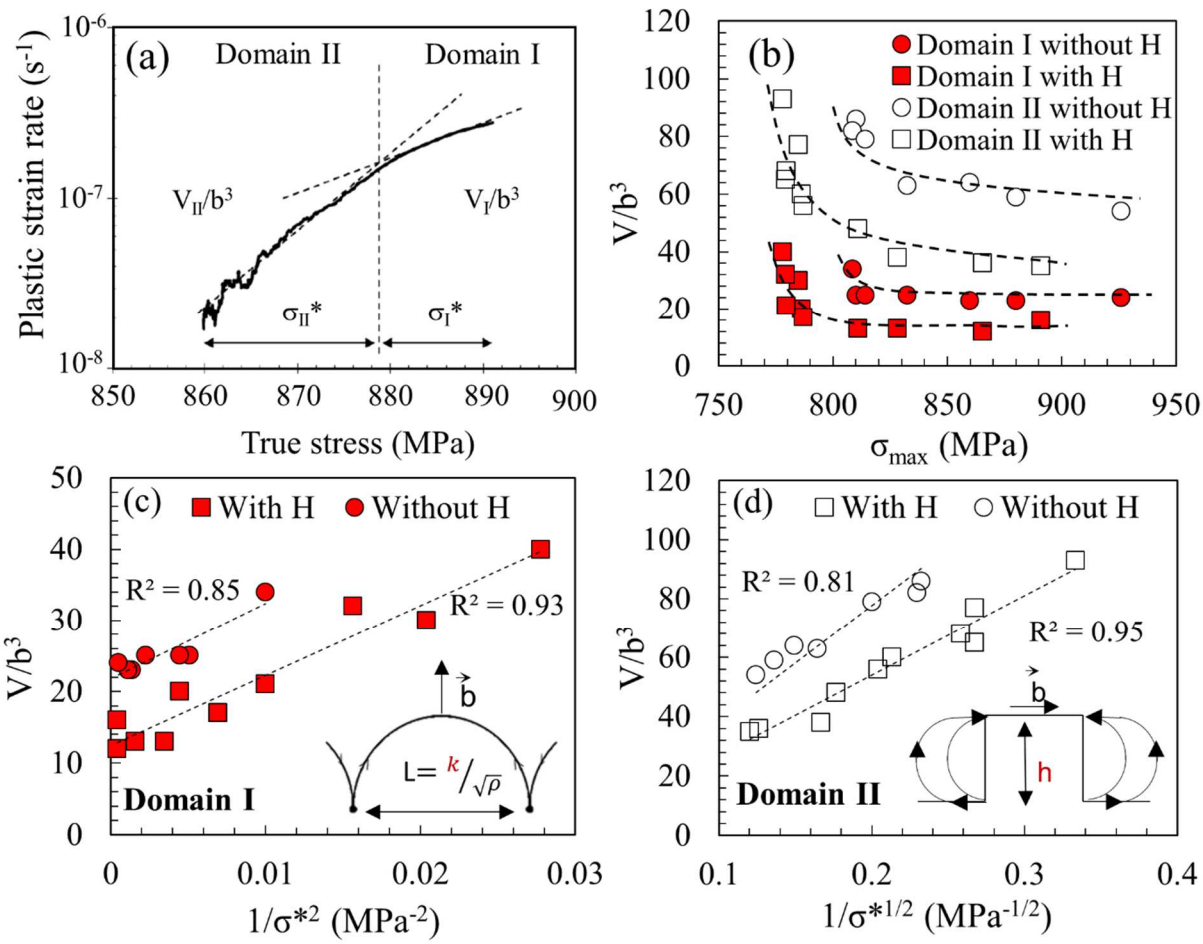


**Figure 12:** Relaxation tests under hydrogen flux (strain rate of $10^{-5}$ $s^{-1}$ and j=100 mA/cm$^2$). (a) Diagram showing the two domains and their associated activation volume and relaxed stress σ* for a maximum stress of 890 MPa, (b) evolutions of activation volume with maximum (peak) stresses for domains I and II with and without hydrogen flux, (c) activation volume with the relaxed stress to the minus 2 for the domain I and (d) activation volume with the relaxed stress to the minus 0.5 for the domain II.

To sum up, in terms of damage mechanism, diffusive hydrogen enhances the mobility of screw dislocations, which increases the dislocation density in the pile-ups and the stress intensity at the interfaces of blocks and/or laths, reducing the stress condition necessary to fracture (Figure 13). A mutual effect of mobile hydrogen and dislocations was identified in this work in agreement with some previous studies [35-37]. Mobile dislocations promote hydrogen diffusion and hydrogen flux favors the movement of dislocations. Both plasticity and hydrogen flux contribute to the quasi-cleavage fracture process as illustrate in Figure 13.

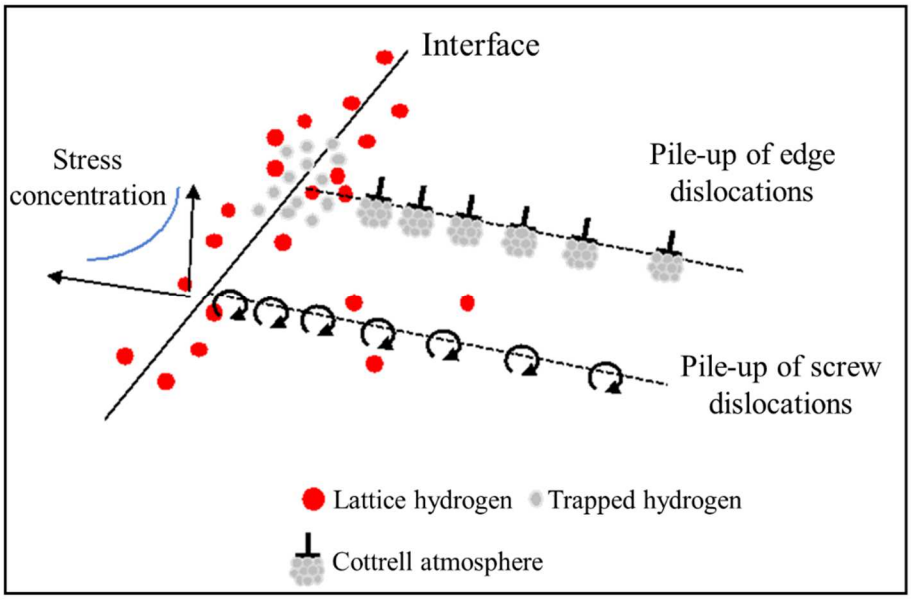


**Figure 13:** Illustration of the three physical processes that promote hydrogen segregation and quasi-cleavage along martensitic interfaces. The hydrogen segregation at the interfaces decrease the interfacial energy. The Cottrell atmospheres near edge dislocations promote the transport of hydrogen to the interfaces reducing further the interfacial energy. The decrease of the activation enthalpy of screw dislocation mobility increase the number of dislocation pile-ups and consequently the stress concentration at the interface favoring decohesion.

## 5. Conclusions

In order to understand the origin of hydrogen embrittlement in the studied martensitic steel, we have separately investigated the effects of trapped and mobile hydrogen. For the mobile hydrogen impact, we have designed an electrochemical permeation device on a tensile machine allowing to control the hydrogen flux until fracture. When only trapped hydrogen is present, the fracture remains entirely ductile and depends on hydrostatic stress, plastic strain and trapped concentration. The hydrogen damage happens by enhancing voids nucleation (reduces the interface energy between precipitate/inclusion and matrix) and growth around inclusions and precipitates. In contrast, mobile hydrogen promotes quasi-cleavage fracture mainly along {101} plans which are lath and/or blocks boundaries. This fracture process depends on hydrostatic stress, plastic strain and hydrogen flux. The plasticity has an important contribution to both HE mechanisms. Specifically, it was shown that hydrogen and dislocations present a mutual interaction. Mobile dislocations drag hydrogen and in its turn hydrogen eases the dislocation

movement by decreasing the activation volume and energy. Both processes favor hydrogen embrittlement.

**Acknowledgements**

The authors thank E. Conforto for her contributions at the microscopy center facilities of the laboratory LaSIE.

**References**

[1] J.F. Newman, L.L. Shreir, Role of hydrides in hydrogen entry into steel from solutions containing promoters, Corrosion Sci. 9 (1969) 631-641.
[2] R.N. Iyer, I. Takeuchi, M. Zamanzadeh, H.W. Pickering, Hydrogen Sulfide Effect on Hydrogen Entry into Iron- A Mechanistic Study, Corrosion 46 (1990) 460-468.
[3] X. Feaugas, D. Delafosse, Hydrogen and Crystal Defects Interactions: Effects on Plasticity and Fracture, in: C. Blanc, I. Aubert (Eds.), Mechanics - Microstructure - Corrosion Coupling, first ed., Elsevier Publisher, 2019, pp. 219-243.
[4] R.P. Gangloff, B.P. Somerday, Gaseous hydrogen embrittlement of materials in energy technologies, first ed., Woodhead Publishing, 2012.
[5] S.P. Lynch, Mechanistic and fractographic aspects of stress-corrosion cracking (SCC), in: V.S. Raja, T. Shoji (Eds.), Stress Corrosion Cracking, Woodhead Publishing, 2011, pp. 3–89.
[6] A. Kimura, H. K. Birnbaum, The effects of cathodically charged hydrogen on the flow stress of nickel and nickel-carbon alloys, Acta Metall. 35 (1987) 1077-1088.
[7] M. L. Martin, B. P. Somerday, R. O. Ritchie, P. Sofronis, I. M. Robertson, Hydrogen-induced intergranular failure in nickel revisited, Acta Mater. 60 (2012) 2739-2745.
[8] A. Oudriss, J. Creus, J. Bouhattate, E. Conforto, C. Berziou, C. Savall, X. Feaugas, Grain size and grain-boundary effects on diffusion and trapping of hydrogen in pure nickel, Acta Mater. 60 (2012) 6814-6828.
[9] D.P. Abraham, C.J. Altstetter, Hydrogen-enhanced localization of plasticity in an austenitic stainless steel, Metall. Mater. Trans. A 26 (1995) 2859-2871.
[10] I. Aubert, N. Sainter, J.M. Olive, Crystal plasticity computation and atomic force microscopy analysis of the internal hydrogen-induced slip localization on polycrystalline stainless steel, Scripta Mater. 66 (2012) 698-701.
[11] A. Nagao, C. D. Smith, M. Dadfarnia, P. Sofronis, I. M. Robertson, The role of hydrogen in hydrogen embrittlement fracture of lath martensitic steel, Acta Mater. 60 (2012) 5182-5189.
[12] J. Venezuela, Q. Liu, M. Zhang, Q. Zhou, A. Atrens, The influence of hydrogen on the mechanical and fracture properties of some martensitic advanced high strengths steels studied using the linearly increasing stress test, Corros. Sci. 99 (2015) 98-117.
[13] T. Das, S.K. Rajagopalan, S. V. Brahimi, X. Wang, S. Yue, A study on the susceptibility of high strength tempered martensite steels to hydrogen embrittlement (HE) based on incremental step load (ISL) testing methodology, Mater. Sci. Eng. A 716 (2018) 189-207.

[14] H. K. Birnbaum, P. Sofronis, Hydrogen-enhanced localized plasticity – a mechanism for hydrogen-related fracture, Mater. Sci. Eng. A 176 (1994) 191-202.
[15] S. P. Lynch, Environmentally assisted cracking: overview of evidence for an adsorption-induced localized-slip process, Acta Metall 36 (1988) 2639-2661.
[16] R. A. Oriani, A mechanistic theory of hydrogen embrittlement of steels, Berichte der Bunsengesellschaft 76 (1972) 848-857.
[17] Y. Fukai, Formation of superabundant vacancies, in: The Metal-Hydrogen System – Basic bulk properties, second ed, Springer, 2005, pp. 216-229.
[18] A. Metsue, A. Oudriss, X. Feaugas, Hydrogen solubility and vacancy concentration in nickel single crystals at thermal equilibrium: New insights from statistical mechanics and ab initio calculations, J. Alloys Compounds 656 (2016) 555-567.
[19] J. Li, A. Oudriss, A. Metsue, J. Bouhattate, X. Feaugas, Anisotropy of hydrogen diffusion in nickel single crystals: the effects of self-stress and hydrogen concentration on diffusion, Scientific Reports 7, n° 45041 (2017).
[20] Y. Fukai, M. Mizutani, S. Yokota, M. Kanazawa, Y. Miura, T. Watanabe, Superabundant vacancy-hydrogen clusters in electrodeposited in Ni and Cu, J. Alloys Compounds 356-357 (2003) 270-273.
[21] M. B. Djukic, G. M. Bakic, V.S. Zeravcic, A. Sedmak, The synergistic and interplay of hydrogen embrittlement mechanisms in steels and iron: Localized plasticity and decohesion, Eng. Fract. Mech. 216 (2019) 106528.
[22] R. Kirchheim, Reducing grain boundary, dislocation line and vacancy formation energies by solute segregation I. Theoretical background, Acta Mater. 55 (2007) 5129-5138.
[23] R. Kirchheim, Revisiting hydrogen embrittlement models and hydrogen-induced homogeneous nucleation of dislocations, Scripta Mater. 62 (2010) 67-70.
[24] I.M. Roberston, H.K. Birnbaum, P.A. Sofronis, Chapter 91: Hydrogen effects on plasticity, in: L. Kubin, J.P. Hirth (Eds.), Dislocations in Solids, North Holland, 2009, pp. 249-293.
[25] I-W. Kang, S-I. Pyun, K-T. Kim, The effects of dislocations on the trapping and transport of hydrogen in 3.3Ni-1.6Cr steel during plastic deformation, Scripta Metall. 23 (1989) 223-226.
[26] P. Sofronis, H. K. Birnbaum, Mechanics of the hydrogen-dislocation-impurity interactions – I. Increasing shear modulus, J. Mech. Phys. Solids 43 (1995) 49-90.
[27] P.J. Ferreira, I. M. Robertson, H. K. Birnbaum, Hydrogen effects on the interactions between dislocations, Acta Mater. 46 n.5 (1998) 1749-1757.
[28] J.P. Chateau, D. Delafosse, T. Magnin, Numerical simulations of hydrogen-dislocation interactions in fcc stainless steels: Part I: hydrogen-dislocation interactions in bulk crystals, Acta Mater. 50 (2002) 1507-1522.
[29] G. Girardin, D. Delafosse, Measurement of the saturated dislocation pinning force in hydrogenated nickel and nickel base alloys, Scripta Mater. 51 (2004) 1177-1181.
[30] S. Wang, N. Hashimoto, Y. Wang, S. Ohnuki, Activation volume and density of mobile dislocations in hydrogen-charged iron, Acta Mater. 61 (2013) 4734-4742.
[31] M. Dadfarnia, M. L. Martin, A. Nagao, P. Sofronis, I. M. Robertson, Modeling hydrogen transport by dislocations, J. Mech. Phys. Solids (2015) 511-525.
[32] T. Magnin, Chapter 5: SCC and CF Modellings Based on Corrosion-Deformation Interactions, Mater. Sci. Forum 202 (1995) 95-132.

[33] A. Nagao, C.D. Smith, M. Dadfarnia, P. Sofronis, I. M. Robertson, Interpretation of hydrogen-induced fracture surface morphologies for lath martensitic steel, Procedia Mater. Sci. 3 (2014) 1700-1705.
[34] I.M. Robertson, P. Sofronis, A. Nagao, M.L. Martin, S. Wang, D.W. Gross, K.E. Nygren, Hydrogen embrittlement understood, Metall. Mater. Trans. A 46 (2015) 2323-2341.
[35] A. Nagao, M. Dadfarnia, B. P. Somerday, P. Sofronis, R. O. Ritchie, Hydrogen-enhanced-plasticity mediated decohesion for hydrogen-induced intergranular and "quasi-cleavage" fracture of lath martensitic steels, J. Mech. Phys. Solids 112 (2018) 403-430.
[36] P. Novak, R. Yuan, B.P. Somerday, P. Sofronis, R.O. Ritchie, A statistical, physical-based, micro-mechanical model of hydrogen-induced intergranular fracture in steel, J. Mech. Phys. Solids 58 (2010) 206-226.
[37] M. B. Djuvik, V. Sihacki Zeravcic, G. Bakic, A. Sedmak, B. Rajicic, Hydrogen embrittlement of low carbon structural steel, Procedia Mater. Sci. 3 (2014) 1167-1172.
[38] R. A. Oriani, The diffusion and trapping of hydrogen in steel, Acta Metall. 18 (1970) 147-157.
[39] F-G. Wei, K. Tsuzaki, Response of hydrogen trapping capability to microstructural change in tempered Fe-0.2C martensite, Scripta Mater. 52 (2005) 467-472.
[40] S. Frappart, X. Feaugas, J. Creus, F. Thebault, L. Delattre, H. Marchebois, Study of the hydrogen diffusion and segregation into Fe-C-Mo martensitic HSLA steel using electrochemical permeation test, J. Phys. Chem. Solids 71 (2010) 1467-1479.
[41] S. Frappart, A. Oudriss, X. Feaugas, J. Creus, J. Bouhattate, F. Thébault, L. Delattre, H. Marchebois, Hydrogen trapping in martensitic steel investigated using electrochemical permeation and thermal desorption spectroscopy, Scripta Mater. 65 (2011) 859-862.
[42] T. Depover, O. Monbaliu, E. Wallaert, K. Verbeken, Effect of Ti, Mo and Cr based precipitates on the hydrogen trapping and embrittlement of Fe-C-X Q&T alloys, Inter. J. Hydrogen Energy 40 (2015) 16977-16984.
[43] J. Takahashi, K. Kawakami, Y. Kobayashi, Origin of hydrogen trapping site in vanadium carbide precipitation strengthening steel, Acta Mater. 153 (2018) 193-204.
[44] T. Schaffner, A. Hartmaier, V. Kokotin, M. Pohl, Analysis of hydrogen diffusion and trapping in ultra-high strength steel grades, J. Alloys Compounds 746 (2018) 557-566.
[45] J. Venezuela, Q. Zhou, Q. Liu, H. Li, M. Zhang, M. S. Dargush, A. Atrens, The influence of microstructure on the hydrogen embrittlement susceptibility of martensitic advanced high strength steels, Mater. Today Communications 17 (2018) 1-14.
[46] A.S. Argon, J. Im, R. Safoglu, Cavity formation from inclusions in ductile fracture, Metall. Trans. A (1975) 825-837.
[47] F. M. Beremin, Cavity formation from inclusions in ductile fracture of A508 steel, Metall. Trans. A (1981) 723-731.
[48] A. L. Helbert, X Feaugas, M. Clavel, The influence of stress triaxiality on the damage mechanisms in an equiaxed α/β Ti-6Al-4V alloy, Metall. Mater. Trans. A (1996) 3043-3058.
[49] S. Frappart, X. Feaugas, J. Creus, F. Thebault, L. Delattre, H. Marchebois, Hydrogen solubility, diffusivity and trapping in a tempered Fe-C-Cr martensitic steel under various mechanical stress states, Mater. Sci. Eng. A 534 (2012) 384-393.
[50] D. Guedes, A. Oudriss, S. Frappart, G. Courlit, S. Cohendoz, P. Girault, J. Creus, J. Bouhattate, A. Metsue, F. Thebault, L. Delattre, D. Koschel, X. Feaugas, The influence of

hydrostatic stress states on the hydrogen solubility in martensitic steels, Scripta Mater. 84-85 (2014) 23-26.
[51] D. Guedes, A. Oudriss, S. Cohendoz, J. Creus, J. Bouhattate, X. Feaugas, F. Thebault, D. Koschel, The influence of hydrogen flux on crack initiation in martensitic steels, Procedia Mater. Sci. 3 (2014) 2024-2029.
[52] E. Legrand, X. Feaugas, J. Bouhattate, Generalized model of desorption kinetics: Characterization of hydrogen trapping in a homogeneous membrane, Int. J. of Hydrogen Energy, 39 (16) (2014) 8374-8384.
[53] V.I. Dotsenko, Stress Relaxation in Crystals, Phys. Stat. Sol. (b) 93 (1979) 11-43.
[54] D. Caillard, Kinetics of dislocations in pure Fe. Part I. In situ straining experiments at room temperature, Acta Mater. 58 (2010) 3493-3503.
[55] A. Shibata, H. Takahashi, N. Tsuji, Microstructural and crystallographic features of hydrogen-related crack propagation in low carbon martensitic steel, ISIJ Inter. 52 (2012) 208-212.
[56] J.L. Chaboche: in Unified Constitutive Laws of Plastic Deformation, A.S. Krausz and K. Krausz, Academic Press, New York, NY, 1996.
[57] A. H. M. Krom, A. Bakker, Hydrogen trapping models in steel, Metall. Mater. Trans. B 31 (2000) 1475-1482.
[58] J. Huez, X. Feaugas, A.L. Helbert, I. Guillot, M. Clavel, Damage process in commercially pure α-titanium alloy without (Ti40) and with (Ti40-H) hydrides, Metall. Mater. Trans. A 29A (1998) 1615-1628
[59] C. Guillemer-Neel, X. Feaugas, M. Clavel, Mechanical behavior and damage kinetics in nodular cast iron: Part I. Damage Mechanisms, Metall. Mater. Trans. A 31A (2000) 3063-3074.
[60] P. Sofronis, R. M. McMeeking, Numerical analysis of hydrogen transport near a blunting crack tip, J. Mech. Phys. Solids 37 (1989) 317-350.
[61] A.H.M. Krom, R.W.J. Koers, A. Bakker, Hydrogen transport near a blunting crack tip, J. Mech. Phys. Solids 47 (1999) 971-992.
[62] A. Brownrigg, W.A. Spitzig, O. Richmond, D. Teirlinck, and J.D. Embury, The influence of hydrostatic pressure on the flow stress and ductility of a spherodized 1045 steel, Acta Metall. 31 (1983) 1141-1150.
[63] A. L. Helbert, X. Feaugas, M. Clavel, Effects of microstructural parameters and back stress on damage mechanisms in α/β titanium alloys, Acta Mater. 46 (1998) 939-951.
[64] D. Francois, A. Pineau, A. Zaoui, Mechanical behaviour of Materials, Solid Mechanics and its applications, Springer editor, (2013).
[65] A. Turk, D. S. Martin, P. E. J. Rivera-Diaz-del-Castillo, E. I. Galindo-Nava, Correlation between vanadium carbide size and hydrogen trapping in ferritic steel, Scripta Mater. 152 (2018) 112-116.
[66] A. Oudriss, A. Fleurentin, G. Courlit, E. Conforto, C. Berziou, C. Rébéré, S. Cohendoz, J.M. Sobrino, J. Creus, X. Feaugas, Consequence of the diffusive hydrogen contents on tensile properties of martensitic steel during the desorption at room temperature, Mater. Sci. Eng. A (2014) 420-428.

[67] W.T. Geng, V. Wang, J-X Li, N. Ishikawa, H. Kimizuka, K. Tsuzaki, S. Ogata, Hydrogen trapping in carbon supersaturated α iron and its decohesion effect in martensitic steel, Scripta Mater. 149 (2018) 79-83.
[68] C. Du, J.P.M. Hoefnagels, R. Vaes, M.G.D. Geers, Plasticity of lath martensite by sliding of substructure boundaries, Scripta Mater. 120 (2016) 37-40.
[69] J. Chêne, A.M. Brass, Hydrogen transport by mobile dislocations in nickel base superalloy single crystals, Scripta Met. 40 (1999) 537-542.
[70] H. Shoda, H. Suzuki, K. Takai, Y. Hagihara, Hydrogen Desorption Behavior of Pure Iron and Inconel 625 during Elastic and Plastic Deformation, ISIJ Int. 50 (2010) 115–123.
[71] Y Lan., H.J. Klaar, W. Dahl, Evolution of dislocation structures and deformation behavior of iron at different temperatures: Part I. strain hardening curves and cellular structure, Metall. Trans. A 23 (1992) 537-544.
[72] J. Friedel, Dislocations, Pergamon Press, Oxford (1964) p. 491.
[73] J.P. Hirth, J. Lothe, Theory of dislocations, Krieger Publishing, (1982), p. 857.
[74] D. Caillard, J.L. Martin, Thermally Activated Mechanisms is Crystal Plasticity, Pergamon Press, Oxfords (2003) p. 433.

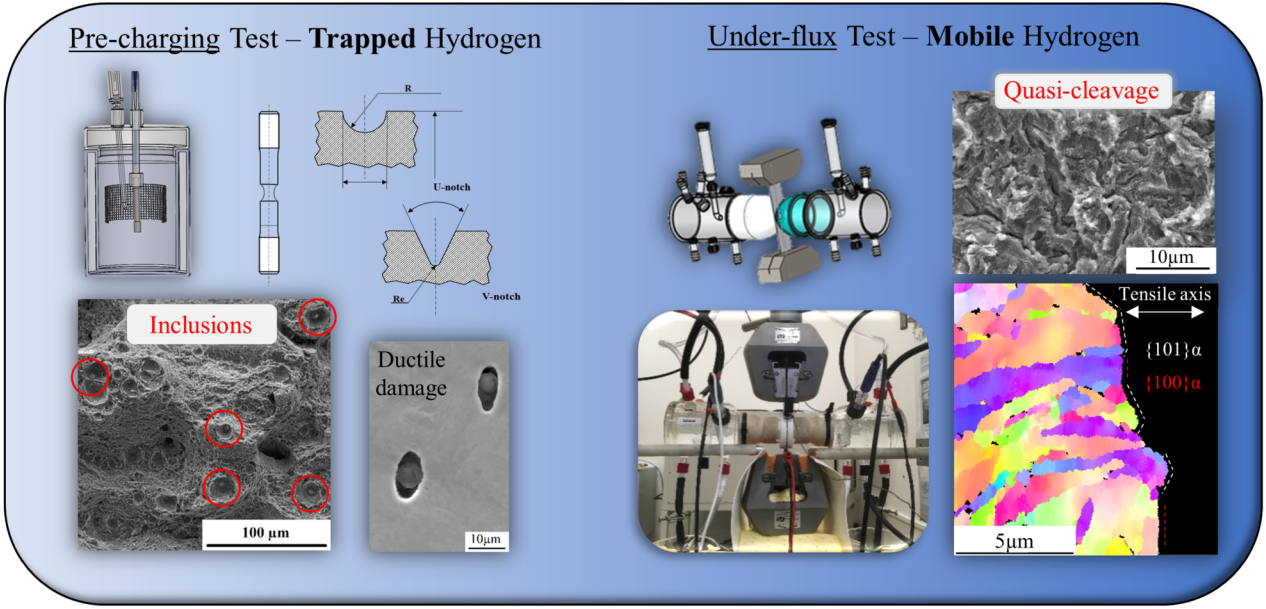
Pre-charging Test – Trapped Hydrogen
Under-flux Test – Mobile Hydrogen
R
U-notch
Re
V-notch
Inclusions
100 µm
Ductile damage
10µm
Quasi-cleavage
10µm
Tensile axis
{101}α
{100}α
5µm